

Contents

1	Introduction to surface forces	5
1.1	Forces between molecules.....	6
1.2	Brownian Motion	7
1.3	Van der Waals Forces.....	8
1.3.1	Electrostatic interactions	11
1.3.2	Lennard-Jones potential	16
1.4	DLVO theory	17
1.5	Hydrodynamic interactions.....	18
1.6	Considering reality	19
1.6.1	Attaching a marble to the ceiling	20
1.6.2	The effects of surface roughness	21
1.6.3	Attaching spherical putty to the ceiling	21
1.7	Bulk vs singular interactions.....	22
1.7.1	Rheology	22
1.7.2	Shear thickening.....	23
1.7.3	Lubrication forces	23
1.7.4	Simple viscous drag.....	23
1.7.5	Rheology of suspended colloidal particles	24

2 Atomic force microscopy	25
2.1 Introduction	25
2.2 Basic overview of AFM operation	26
2.3 Imaging mode AFM	28
2.4 Tip Calibration	29
2.5 Mathematical alignment and error	30
2.6 Force microscopy	32
2.7 Tip calibration	33
2.8 Application of Derjaguin approximation	34
3 Surface Imaging	35
3.1 Introduction	35
3.2 Silica particle surface resolution.....	38
3.3 Root mean squared roughness.....	39
4 Atomic force spectroscopy analysis	40
4.1 Introduction	40
4.2 MFP-1D	40
4.2.1 Experimental setup	42
4.2.2 MFP-1D force-distance curves acquisition and processing....	45
4.2.3 Validation of results	51
4.3 Nanowizard	52
4.3.1 Analysis differences for JPK NanoWizard.....	53

5 Approach force curves	54
5.1 Introduction	56
5.1.1 0.6mM	57
5.1.2 1.6mM	59
5.1.3 5mM.....	61
5.1.4 10mM	63
5.1.5 25mM	64
5.1.6 50mM	65
5.1.7 230mM.....	66
5.1.8 550mM.....	68
5.2 Effects of hydrodynamics	70
5.3 Dwell time effects.....	72
5.4 pH effects.....	75
5.5 Force mapping.....	76
6 Retract force curves	77
6.1 Introduction	77
6.1.1 0.6mM	78
6.1.2 1.6mM	80
6.1.3 5mM.....	82
6.1.4 10mM	84
6.1.5 25mM	85
6.1.6 50mM	86
6.1.7 230mM.....	87

6.1.8	550mM.....	89
6.2	Effects of hydrodynamics	91
6.3	Dwell time effects.....	93
6.4	pH effects.....	96
6.5	Force mapping.....	98
7	Force event analysis and conclusions	99
8	Bacterial colloids AFM	100
8.1	Introduction	100
8.1.1	AFM tip treatment	100
8.1.2	Attaching bacteria to a cantilever.....	100
8.2	Bacterial force curves.....	101
9	Conclusion	102
Bibliography		103

Chapter 1

Introduction to surface forces

As matter encroaches upon one another,

These forces and mechanisms are known as interacting surfaces forces, and the interplay of these interactions define the systems we experience and observe in day to day life. Some examples include the wetting of surfaces from an interfacing liquid or the means in which an organism adheres to a surface.

These forces, while from the perspective of the universe are nothing new, have gained increasing interest and understanding over the last century to scientists and industry alike. The demand for a clear and concise picture of these interactions only increases as innovations in technology rely more and more on these interactions, from touch screen developments, water resistant superhydrophobic surfaces, bacterial frustrating surfaces or even the humble custard.

There are several ways to flirt with these forces either as an innovator; either by chemically treating the surface, altering the physical structure of said surface or by altering the interfacial solute said surface finds itself involved with. By changing these properties new promising technologies can push our understanding of such a system to it's limits.

As scientific study becomes more and more involved on elucidating these interactions on the molecular scale, we find more and more of the world we live in defined by our understanding of such systems and as a result, it is imperative to not only question the history of our combined understanding, but to test such systems experimentally.

The history of surface forces finds itself derived from van der Waals forces, a theory produced by a series of papers produced by London, Debye and Keesom [22]. These attractive forces were combined with repulsive double layer forces to form the main theoretical basis of particle-particle interactions, consequently known as DLVO (derived from Boris Derjaguin and Lev Landau, Evert Verwey

and Theodoor Overbeek) as a result of two groups reaching the same conclusion independently[38][10]. This underlying theory describes the resultant surface forces felt between two particles in solution .

From these simple particle-particle interactions bulk behaviours are derived, such as the case for colloidal systems. Mixed phase suspensions, called colloids are a combination of a solvent and a solute. Indeed, one only has to look inwards to find a fascinating colloidal system (albeit a very complicated one). [15] [14]

Systems defined by intermolecular forces are prevalent in a wide range of applications, said theory providing the basis for several industries such as water purification, batch processing (food, pharmaceuticals, detergents, paints) and mining.[36]

1.1 Forces between molecules

Intermolecular forces are essentially electrostatic in nature, as postulated from quantum theory, initially defined by the Hellman-Feynman theorem. From the Coulomb force and complex fluctuating forces observed around the surfaces of atoms. However, simple solutions to the Schrödinger are hard to come by, and as such, this unified force is fractured down into small classifications to simplify their definition and equation. These categories are known as ionic forces, van der Waals forces, hydrophobic forces, hydrogen bonding and solvation forces.

Chemical bonding depends on the interaction of neighboring atomic orbitals, while steric forces arise from quantum mechanical or electrostatic interactions between separated particles. They are an emergent property of the electronic structure of the atoms, as opposed to a molecular orbitals, where the molecular configuration is in a state of semi-permanence and free from flux changes.

A main difference between the two is the permanence of charge distribution changes, where in the case of the former is retained as long as the bond is retained.

Coulomb forces are the force of the charge effects of two charges applied upon one another with respect to distance.

In approximation the inverse square force is given by:

$$F \propto \frac{Q_1 Q_2}{kr^2} \quad (1.1)$$

Where upon this can be expanded into:

$$F = -\frac{dw(r)}{dr} = \frac{z_1 z_2 e^2}{4\pi \epsilon_0 \epsilon r^2} \quad (1.2)$$

where $w(r)$ is the free energy of the Coulomb interaction, r is the distance between the two charges Q_1 and Q_2 . ϵ is dielectric constant of the medium, and z is the ionic valency of the atom in question, in relation to the elementary charge e . Due to its inverse square law nature it is a force highly dependant on distance.

1.2 Brownian Motion

Traditionally; the term colloid was coined in 1861, drawn from the Greek word (kolla), meaning glue, from Thomas Graham's observations of aggregation[17]. Nowadays a colloid is defined as the intermixing of two separate phases; a dispersed, suspended phase and a continuous, medium phases in which the former find themselves in. For our area of interest, we place our scope on a particular colloidal suspension; a dispersion of solid particles within a liquid medium. [?]

Consider the idea of marbles kept within a liquid. At rest, they would lie upon the bottom of the container, yielding to the force of gravity[?]. However, as you scale down these marbles, to smaller and smaller sizes, the kinetic energy of the system is enough for keep the marbles dispersed within the liquid, due to Brownian motion[?].

At micrometer sizes however, the marbles begin to affect one another; when two marbles are brought together by Brownian motion, provided the interactions between the two of them are attractive, they will attract towards each other, and eventually aggregate, until they are large enough to sediment again. If there is no attraction, or indeed repulsion, between the marbles, they will stay suspended within the solution.

Interactions between the marble's surfaces, are defined by a few fundamental forces resolving linearly with one another. These interplay of forces, borne from electrostatics, van der Waals and solvation forces, all sum up into a force profile based on distance between the two surfaces.

These force profiles depend upon a number of intrinsic properties to the phenomena. To define these variables in a broad stroke; the liquid the solid colloid is immersed in (liquid phase properties), the surface properties of the solid phase (solid phase properties) and interactions between same phase particles (same phase interacting properties).

On the macro scale, these interactions equal out to resolve into their bulk properties. As this system is disturbed by external forces, a resultant relaxation time is observed, dependant on the ions in solution and surface properties of the solid phase particles. From these disturbances, new dipole moments can arise additionally. These properties give rise to the hysteretic effects seen in systems such as these.

With such a complex system of non trivial interactions, the history of elucidating

such a complex system has not been a simple one. Ideally in physics finding a unifying, complete equation to describe all manner of interactions would be the goal, however, even if that were possible, colloidal systems are not frozen in an equilibrated state and are the result of combining relations between intrinsic properties and dynamic, sympathetic effects. As such the current state of the theory relies upon simplified simulations to push forward the field, and as such, an experimental analysis upon said models is required. [21][27]

1.3 Van der Waals Forces

The predominant attractive force applied upon the solid phase of a colloidal system is van der Waals attractive forces.

Originally recognised by Johannes Diderik Van der Waals, of which the name derives from, in 1873 [42] it was only later in 1930 that these forces were defined by London in 1930[12] almost 60 years later into what is known as London dispersion forces.

These forces can be further broken down into three types; Keesom forces (aka permanent dipole - permanent dipole interactions), Debye forces (aka permanent dipole - induced dipole interactions) and dispersion forces (aka induced dipole - induced dipole interactions). [19]. Keesom forces derive from the permanent charge nature of atoms, where a static dipole induces an attraction between two particles, due to their stable differences in charge (see fig 1.1). These fluctuating motions present in these permanent dipole moments result in the $1/r^6$ interaction potential even with these other sources.

Dispersion forces act between all atoms and molecules, even present in neutrally charged elements, thanks to their quantum mechanical nature. To explain how these forces arise, consider an atom. While the time averaged dipole moment is zero, due to the changing position of its electrons around its positively charged nucleus, it has a fluctuating non-zero, instantaneous dipole moment. This fluctuating instantaneous dipole moment generates a fluctuating electric field on any neighboring neutral atoms. The interaction between the instantaneous dipole moment in atom one and the induced dipole in atom two, averaged over orientation to account for the fluctuating nature of the instantaneous dipole, gives rise to an attractive interaction between the two atoms. The electric field from instantaneous dipole falls off with distance as $E_{\text{ins}} \propto 1/r^3$, and the induced dipole moment is proportional to this field, $p_{\text{ind}} \propto \alpha E_{\text{ins}}$ with α to polarizability of the second atom. The interaction energy is then $U \propto p_{\text{ind}} E_{\text{ins}} \propto 1/r^6$.

These forces have been described as dispersion forces, London forces [12], dipole-dipole forces, all attributing to their origin; a dispersion force caused by an electrodynamical charge flux inducing dipole moment. These dispersion forces make up one of three types of forces contributed by van der Waals forces and is

ubiquitous, unlike the other two sources, which depend on their permanent dipole properties and the nature of the medium. [27]

[18] [27] [21]

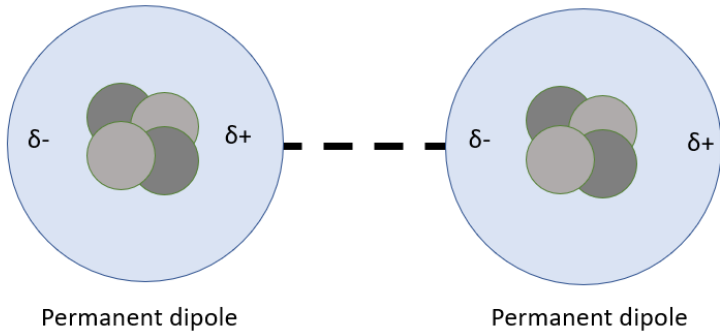


Figure 1.1 A basic schematic of Keesom interacting forces.

Debye forces instead induce a dipole moment in a nearby atom, causing a sympathetic response from the permanent dipole (see fig 1.2). This quantum mechanical phenomena arises from fluctuations of the electrons on the surface, resulting in an averaged δ positive force on the induced atom, from the localised departure of electrons away from the inducing atom.

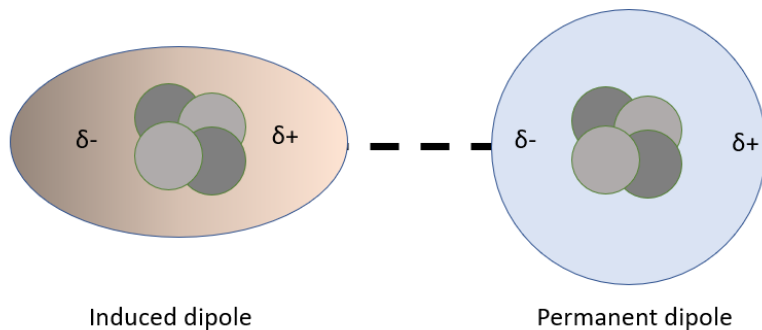


Figure 1.2 A basic schematic of Debye interacting forces.

dispersion interacting forces (see fig 1.3)

Van der Waals forces make up the dominant attractive force between macroscopic colloids, however, the operational distance of the force is very short ranged, as it relies heavily on induced dipole fluctuations on the surfaces between particles. [24] This interaction can be described by equation 1.3:

Mathematical basis of dispersion forces

$$U_{vdW}(r) = -\frac{Ar}{12hkT} \quad (1.3)$$

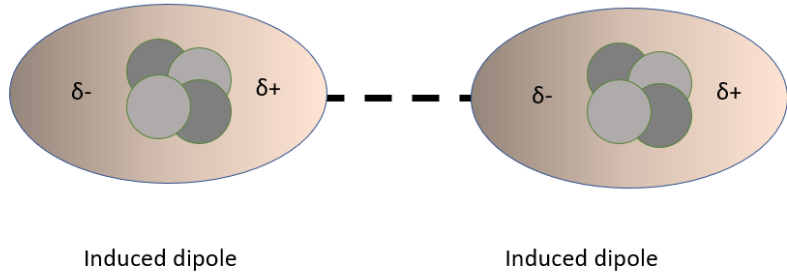


Figure 1.3 A basic schematic of dispersion interacting forces.

$$U_{vdW}(r) = -\frac{A}{12\pi} \left(\frac{R}{r}\right)^2 \quad (1.4)$$

U being the attractive cohesive energy, A is the Hamaker constant, R is the radius of the colloidal particle, assumed to be of equal radius for the other particle, r distance between the two particles.[?] A is calculated by:

$$A = \pi^2 C p_1 p_2 \quad (1.5)$$

Where C is the interaction parameter, given by the coefficient in the particle-particle pair interaction. p_1 and p_2 are the number densities of two interacting kinds of particles.[?] C is calculated by:

$$w(r) = -\frac{C}{r^6} \quad (1.6)$$

where $w(r)$ is the pair interaction energy between two particles.

One striking element of the derived interaction energies between colloidal particles is it's heavy reliance on distance, where they are only effective up to tens of nanometers. When colloids in a solvent are considered, it is important to note that A will change with respect to the solvent it finds itself in, and the colloidal particle's properties.[?]

1.3.1 Electrostatic interactions

When two phases interface with one another there is a known tendency for ions to arrange along the interface in order to reduce the free energy of the system. These resultant electric fields from the ions may induce polarisation effects in nearby molecules. These combined effects result in an electric potential difference between the two phases.

Coulomb's law attempts to explain the force experienced between two electrically charged particles suspended in motion. This force is usually referred to as electrostatic force or Coloumbic force.

$$F = \frac{q_1 q_2}{4\pi e_0 r^2} \quad (1.7)$$

This law describes the force applied to two particles with electric charge q (q_1 and q_2 respectively), where e_0 is the vacuum permittivity. In the case where the particles are in solution, this is replaced by ϵ - the dielectric constant, given by:

$$\epsilon = \frac{e}{e_0} \quad (1.8)$$

Where e is the electron charge. If the sign of q_1 and q_2 are the same, then it is a repulsive force, otherwise it is attractive. $4\pi e_0$ is sometimes simplified to the electrostatic constant.

Charges on surfaces can arise due to several different phenomena:, The innate surface chemistry, the adsorption of ions from the solution onto the surface and dissociation of surface ions into solution.

Surfaces can also be affected by charge in a range of different ways. Surface chemistry ionisation can occur based upon the solvent pH, where acidic or basic groups can dissociate away from the surface and into the solution. The surface has a positive charge in the case of a basic surface, and a negative in an acidic. One way to manage this property is to control the pH of the solution.

The charge present upon a surface attracts counter ions, which associate towards said surface. This phenomenon is known as charge screening and is dependant on ionic salts within the aqueous solution. [?]

Charge screening

As ions seek to stabilise themselves within a solution and reduce the free energy of the system an ionic atmosphere surrounding any inversely charged surface will develop over time. Counter ions will move towards the attractive force from the surface, while same charge-ions will be repelled away from the surface. This resulting atmosphere is often referred to as the electrical double layer. As these ions rely on thermal motion to graduate towards the negative surface, it is this thermal energy that causes the ions on the surface to diffuse slightly from direct contact.

One way to reduce the charge barrier from the surface is to introduce an contrary charged ion, inverse of the colloidal surface charge, to the liquid medium. As these ions stabilise in the system they are inevitably attracted towards the counter

charged surface of the colloid, and settle around them as a "cloud". Thus, the concentration, charge and valence of the ionic salts will change the repulsive forces upon interacting colloids.[?]

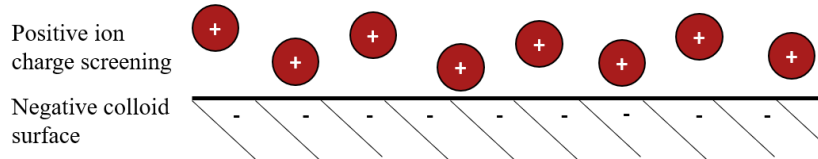


Figure 1.4 A schematic of counter ion distribution under the Gouy-Chapman model. This demonstrates how positive counter ions will arrange themselves around a negative surface.

These ions are subjected to an electrostatic potential (Ψ) as they get closer towards the oppositely charged surface. The positive counterions (see fig 1.4) are attracted by the electric field generated from the negatively charged surface producing a potential seen in fig ??.

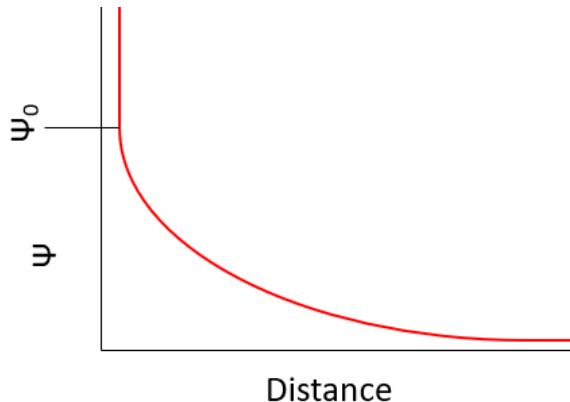


Figure 1.5 The Electrostatic potential of a counter ion, where distance is the distance between the negative surface and positive ion.

In addition to this attractive force upon the ion, the ions are additionally subjected to thermal motion. This thermal motion distributes said ions uniformly throughout the aqueous solution. The result of these combined forces is that the surface of the colloid is surrounded, but not saturated, by said counterions, where they gradually reduce in concentration until reaching bulk concentration levels. This phenomena is termed the diffuse electrical double layer which is highly dependant on the electrolytes in solution.

This double layer phenomena has several models attributed to it. One of the earliest theories put forwards was the Helmholtz model in 1853. This theory puts forward the idea of a simple charge distribution contrary to the surface charge along a planar distribution. This distribution is a function of the distance away

from the surface, and thus surface charge. While this model provided a basis of understanding the interactions between solvent ions and surface charges as a function of distance, it was unable to account for the effects of kinetics on the system. Under this system it was anticipated that the counter ion concentration would increase with proximity to the surface charge, with same charge ions inversely affected.

This model was then revised under the Gouy-Chapman model in 1910-1913, [?] which pays respect to the thermodynamic nature of the system. Which relies on a linearised and approximated Poisson-Boltzmann equation which assumes a uniform surface charge. Equally it assumes that the dielectric constant of a solution is homogeneous, implying that all ions form a diffuse point charge layer and thus ignore discrete ion binding sites.

It is worth noting that the only variables within the equation are from temperature and electrolyte concentration, outside of the constants.

The measure of the effect of this layer The Debye length (λ_D or κ^2) represents the distance beyond which the electrostatic force between charged particles is insignificant.

$$\lambda_D = \kappa^{-1} = \sqrt{\frac{\epsilon_r \epsilon_0 k_B T}{2 Z^2 e^2 n_b}} \quad (1.9)$$

Where ϵ_0 is the vacuum permittivity, k_B is boltzmann constant, T is Temp in K) ϵ_r is the relative dielectric constant, e is the elementary charge, Z is the charge number of the ions in solution and n_b is the number density of the ions. The number density is given by:

$$n_b = N_A \frac{\text{moles}}{\text{Volume}} \quad (1.10)$$

Where N_A is Avogadro's constant. This can be further simplified to:

$$\lambda_D = \kappa^{-1} = \sqrt{\frac{\epsilon_r \epsilon_0 k_B T}{2000 N_A e^2 I}} \quad (1.11)$$

Where I (the ionic strength) is calculated using:

$$I = \frac{1}{2} \sum c_i z_i^2 \quad (1.12)$$

This characteristic length-scale is then split up into two smaller layers, known as the Stern and diffuse layer.

The Stern layer is comprised of counterions

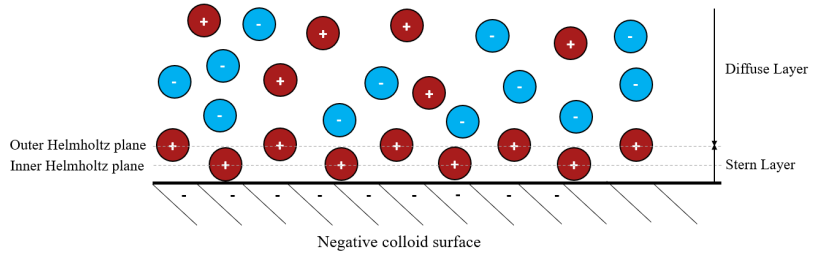


Figure 1.6 The Electrical double layer model highlighting the transition between the Stern and diffuse layers.

Within this region there is a volume of liquid that is unique to the bulk properties of the liquid phase. This region with a higher concentration of counter ions is called the Helmholtz region and is further split up into two parts. The closest to the surface being the inner Helmholtz plane - where ions are adsorbed onto the surface, and the outer Helmholtz layer contains solvated ions. Afterwards the diffuse layer is made up of unbound free ions influenced by Brownian motion.

Electrostatic repulsion

Without the presence of electrostatic repulsion, these particles would surely aggregate together. These repulsive forces arise from the electric charges on the surface of the particle in question, with the strength of these forces varying to the medium they find themselves in.[?] The electrostatic energy of this repulsion is given by:

$$U_E(r) = 4\pi\epsilon R\Psi_0^2\epsilon_0 e^{-\kappa h} \quad (1.13)$$

ϵ being the dielectric constant of the solvent, Ψ_0 being the surface electric potential of the colloid, σ is the surface charge density and κ is the Debye-Hückel constant, or Debye length, defined by:

$$\kappa^{-1} = \left(\frac{\epsilon_r \epsilon_0 k_B T}{2 N_A e^2 I} \right)^{\frac{1}{2}} \quad (1.14)$$

$$n_b = N_A (\text{moles}/m^3) \quad (1.15)$$

$$\lambda_D = \kappa^{-1} = \sqrt{\frac{\epsilon_r \epsilon_0 k_B T}{2000 N_A e^2 I}} \quad (1.16)$$

$$\kappa^{-1} = \sqrt{\frac{k_B T \epsilon_r \epsilon_0}{2 N_A e^2 I}} \quad (1.17)$$

e being the electron charge, n_{oi} is the concentration and $k_b T$ being the thermal energy of the system (Boltzmann's constant plus temperature) [?]. The Debye length is the lengthscale of screened electrostatic repulsions.[?]

$$\Psi_0 \approx \frac{\epsilon_r \epsilon_0 \kappa}{\sigma} \quad (1.18)$$

c_i is the ionic concentration z_i is the valence of i ions.

1.3.2 Lennard-Jones potential

One of the simpler ways to model particle-particle interactions is using a Lennard-Jones potential. This originally sought to model interactions between two noble gas atoms by describing Pauli repulsion coupled with an attractive long range term. This provides a simplistic view by assuming all interactions between all particles are the same, and thus the solution is homogenous. This is done by summing the contributions from all particles interacting with one another. For each interaction the attraction is given by the Van der Waals attraction (See equation 1.4). The repulsive term is given by:

Further simplification can be done in the following form:

$$U = 4\epsilon_{min} \left[\left(\frac{r_0}{r} \right)^{12} - \left(\frac{r_0}{r} \right)^6 \right] \quad (1.19)$$

Insert Lennard's potato

This removes the need for the A and B constants, instead expressing the relationship using the depth of the potential well (ϵ_{min}) and the distance at which the potential is 0 (r_0).

While Lennard-Jones potentials give a good estimation of bulk effects of molecules interacting, it has several limitations. For one it requires homogeneity of both molecules, as well as ignoring any solvent effects. Additionally, its estimation is independent of charge, which plays a larger role when ions within the solvent are present. In particular the Hamaker constant and A' is derived assuming vacuous conditions, whereas it is known that particles immersed within a solvent experience a reduced attractive force. []

In order to improve upon the basics laid out here, these factors need to be considered mathematically. To this end, electrostatics are introduced and considered.

1.4 DLVO theory

These electrostatic $U_E(r)$ repulsions interplay with the van der Waals attractive forces, producing a sum force upon the colloid. This interaction, much like a dance, sways back and forth between attractive and repulsive dominant forces. These two forces were unified into a single theory known as Derjaguin, Landau, Verwey and Overbeek theory (DLVO), named as such based upon the authors in 1943 and 1948.[?] [39] [11]

The context of the initial theory was done upon lyophobic colloids, which is to say a colloidal suspension of particles in a medium that does not precipitate. Particles are prevented from merging (coalescence) and separating via repulsive forces present between one another, and as a result in an equilibrated state it is stable. This repulsion is produced due to the repulsive electrostatic forces described in 1.1.2, present due to the surface charges of the colloid. The attractive forces of the equation result from van der Waals forces present from the electron distribution of the atomic core, from the molecular surface of the colloid, described in 1.1.2.[?]

These two forces combine to produce a defining interaction potential.

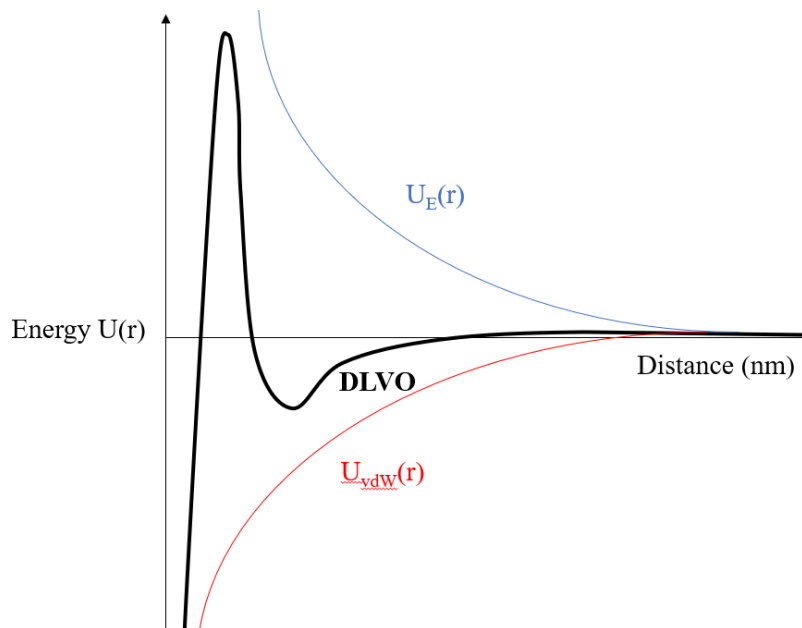


Figure 1.7 A graphical demonstration of the competing forces between colloidal particles. The electrostatic repulsion ($U_E(r)$) and the van der Waals attraction $U_{vdW}(r)$ combine together the sum interplay known as DLVO theory (bold line).

One common feature of DLVO is the repulsive barrier that is seen from the initial dip. This energy barrier prevents colloids from agglomerating. The van der waals forces are generally attractive due to the nature of their interactions at longer

ranges, giving rise to the initial dip, before the electrostatic repulsion dominates, giving said barrier. However, after this energy barrier is broken, the attraction descends to infinity, demonstrating a very strong attraction. If this barrier is enough to prevent colloids from naturally overcoming it due to Brownian motion and thermal energy, then they will remain stable in solution, though, given infinite time it is likely that the solution will aggregate and settle in its lowest energy state where $r = 0$, assuming a perfect sphere.[?]

While DLVO has proven itself a functional and applicable model for the description of interacting colloids, there remains a few assumptions that can cause a divergence from the truth. DLVO assumes that the interacting surfaces is perfectly flat, expanding in all directions, and that the surface charge density is uniformly distributed along said surface. Additionally, it assumes that the surface electric potential is constant, and that any counter ions remain static and uniformly distributed too, with any interactions between said ions or solvent being purely born from their dielectric constant. While some of these assumptions aren't true for particle-particle interactions, DLVO holds up as a theory for predicting interactions. [9] [44] [23] [32] [29]

1.5 Hydrodynamic interactions

The forces discussed prior outline forces that occur when no external forces are applied to the system, and as such the thermodynamical properties are kept time dependant. However, if a force is applied upon the system, then it induces movement locally, and this force precipitates into the rest of the system via hydrodynamical effects. (fig) As the particles within a fluid move, they leave a flow in their wake, which exhibit a force upon other particles and the containing object.

Assuming there is a force applied within the system, this can precipitate out into the rest of the system and can be calculated, provided that one of three assumptions can be made linear flow and constant velocity V_o .

The force applied upon any single particle under those conditions is given by:

$$F_H = 6\pi\eta\alpha v_0 \quad (1.20)$$

η being the intrinsic viscosity of the fluid. F_H is also known as the Stokes drag, provided that the colloidal particles have enough distance to ignore any interparticle hydrodynamic effects.[?]

Steric forces

long range forces

The other way to alter colloid-colloid interactions is to sterically hinder them. By frustrating attractive movement towards one another, they are physically unable to come into contact, and therefore descend towards $r = 0$. Generally, steric hindrance arises from polymeric brushes chemically grafted upon the surface of the colloid, but can also arise from larger molecules in the medium interacting with the surface. For polymeric attachments, they reach out of the colloid as an attempt to reduce the free energy in a system, giving rise to the colloquialism known as polymer brushes. This loss in entropy caused by the brushes frustrating the colloid's freedom of movement causes an increase in the free energy of the system, inciting the colloid's movement away from the other interacting one. Additionally, molecules and particles upon the surface can physically prevent movement of particles towards each other, preventing r from reaching 0.[?]

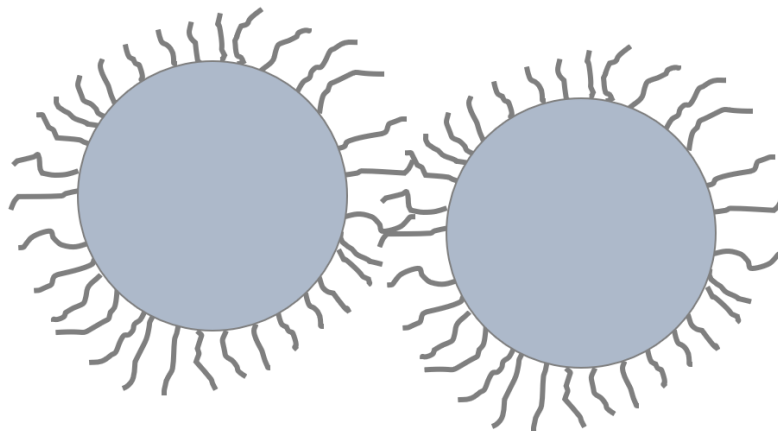


Figure 1.8 *The polymers off the surface of the colloid sterically inhibit any interactions.*

These intermolecular forces define how particles interact on the micro scale, summing into a distance-force profile between particles. As you draw the scope out from two particle interactions, towards macroscale, multibody systems, you start to enter the realm of rheology.

1.6 Considering reality

When you take this model to the extreme example of

1.6.1 Attaching a marble to the ceiling

$$\begin{aligned} mg &= F_{vdW} \\ \rho \frac{4}{3}\pi a^3 g &= \frac{A_H a}{6h_m^2} \\ \rightarrow a &\simeq \sqrt{\frac{3A_H}{24\pi\rho gh_m^2}} \\ &\simeq \sqrt{\frac{10^{-20}J}{24(200kg/m^3)(10m/s^2)(10^{-10}m)^2}} \\ &\simeq 1.4mm \end{aligned}$$

1.6.2 The effects of surface roughness

[copy section here]

1.6.3 Attaching spherical putty to the ceiling

Pressure-sensitive adhesive

viscoelastic

1.7 Bulk vs singular interactions

1.7.1 Rheology

As these small scale forces are applied to one another, across the bulk of the solution, with multiple forces applied from multiple directions, the overall clarity of the forces at play begins to obfuscate. It becomes very difficult to observe in detail the individual mechanisms of particle-particle interactions. As such, either rheological techniques are used for in vitro examination, or the in use of simulations. Rheology itself studies the flow and deformation of a bulk liquid solution under different forces, of which colloids are known to play a part. Oobleck, a well known solution, displays shear thickening properties under shear stress, born from the interplay of forces between the sol colloidal nature of the solution.

While Rheology relies on deriving it's understanding of such systems from a macroscopic lens, simulations takes the current theory underpinning current scientific understanding to build up a theoretical landscape imitating reality. This in silico landscape often relies on Stokesian dynamics to simulate particle-particle interactions across all of the simulation. Simulations work by drawing a defined box with either periodic or constrained boundary conditions, in two or three dimensions, where each particle's sum force is calculated base upon the other particles within the box. Then, afterwards, the frame of reference is shifted forwards a certain amount of time, with the particle's positions moved based upon the last frame's force. This tick happens over and over, with the total time and accuracy dependant on the delta timestep.

Stokesian dynamics involve the use of

1.7.2 Shear thickening

Shear thickening occurs when disperse colloidal particles are subjected to a high shear force, leading to an increase in the observed viscosity.

why here

Also mention that these interactions are determined by intermolecular forces on the nanoscale.

1.7.3 Lubrication forces

Lubrication forces are thought to be the dominant force regarding intercolloidal interactions, causing their observed behaviour and structure (for systems with a high colloidal concentration). These forces arise from small, thin lubricating layers between two particles. This layer is thought to prevent physical contact, and thus frictional forces, between two interacting colloids. From this postulation, the infinite force at $R = 0$ problem is solved, as the colloids never come into contact, instead separated by the viscous, lubricating layer between them during flocculation. Because of this, the particles are able to separate when the shear force is removed, giving the characteristic viscosity shift back and forth.

?

However it is important to note that this theory relies on said particles being perfectly spherical.

1.7.4 Simple viscous drag

1.7.5 Rheology of suspended colloidal particles

As you scale up the viscosity of a liquid and start applying these forces from the microscale to a collective sum on the macroscale you start to see interesting behaviours arise from the fundamental forces intrinsic to the

Chapter 2

Atomic force microscopy

2.1 Introduction

The origin of the microscope is birthed from optics, originally back to the thirteenth century, deriving from eyeglasses and spectacles. The first optical microscope used visible light to image samples by passing photons through them, however as microscopy design improved, the diffraction limit of photons was eventually reached. In order to overcome this limit new techniques were discovered and produced in order to allow different types of images to be produced. Some examples include phase contrast microscopy, electron microscopy and Atomic Force Microscopy (AFM).

One of AFM's largest differentiations from other microscopy techniques is that it relies on physically probing a surface to generate an image. [8]

The first progenitor of the atomic force microscope was invented in 1981, then known as the scanning probe microscope.

Instead of relying on matter or energy to pass through an object a physical tip is brought into contact with a surface. By using a nanometer sharp stylus mounted on a cantilever the surface of a sample can be mechanically probed. The method is novel compared to conventional microscopy techniques as it does not rely on lenses for observation; instead the position of the stylus is detected by a laser reflecting off the surface of the cantilever. By probing the surface of a specimen the surface characteristics can be observed such as the hardness or elasticity of a sample. AFM can be further functionalized with specific tips or attaching specific molecules to detect surface chemistry, adhesion or arrangement of ions on a surface[13].

One of AFM's greatest strengths is the ability to resolve images at nanometer length scales past the optical diffraction limit of standard microscopy techniques. Since AFM's resolving power is limited depending on the radius of the tip different

tips can be used depending on the application, such as nanometer sharp tips to resolve on the atomic scale or tips for use in liquid conditions. A further strength is the ability to image specimens under different conditions; within air, water, or especially in the case of biological samples; within buffers to reduce the adverse effects of observing the samples. [20].

Another boon the AFM provides to its operator is the ability to measure small forces acting between the tip and the probed surface. This interaction is measured over distance, giving a detailed surface force profile at different separation distances.

2.2 Basic overview of AFM operation

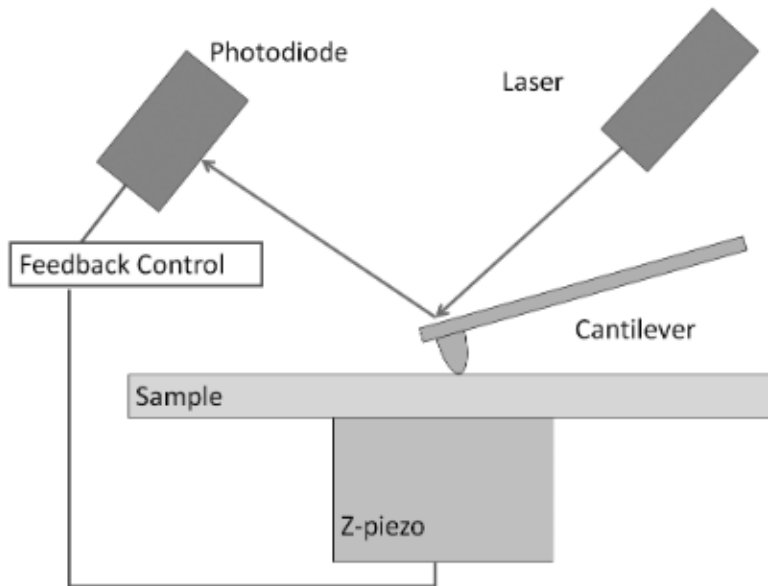


Figure 2.1 A basic schematic of an set up AFM. Image adapted from [43].

The general schematic of an AFM is given in figure 2.1. A laser is emitted and aligned to the head of the cantilever, above the tip. This laser is then reflected off the tip into a photo diode, initially the laser is set up to reflect into the origin position (the center) of the photo diode. As the tip is brought into contact with the surface the tip bends and relaxes altering its reflected angle depending on the underlying sample surface topography. The cantilever is moved by a piezoelectric motor, with emphasis on accuracy of the z-axis sensitivity (most AFMs cite the error on the z-axis to be within the order of magnitude of an angstrom). For the most basic of AFMs the movement of the reflected laser is recorded by a computer along with the sum and the piezo voltage.

As the tip is brought into contact with the surface, various forces are applied

upon the tip, in an example case the total force applied to the cantilever is a combination of Van-der-Waals attractions and electrostatic repulsion, with the resultant force depending on the separation distance of the tip from the surface, h .

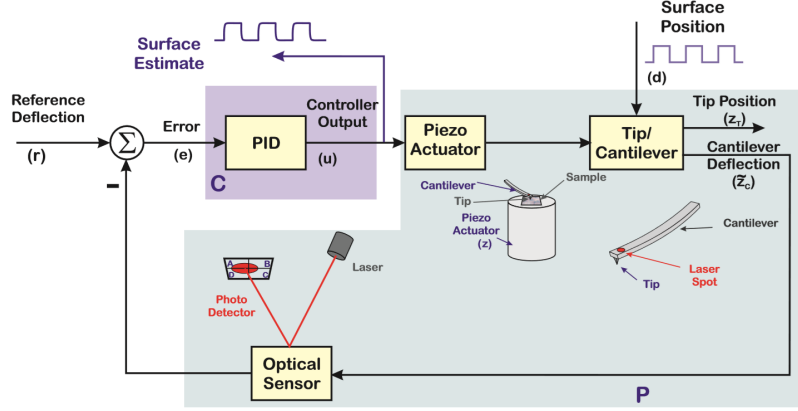


Figure 2.2 A diagram demonstrating the basic feedback loop control for an AFM. In this case an example for an AFM operating in imaging scanning mode is shown, which is elaborated in the next section. Image adapted from [1]

From this interaction, the cantilever is controlled in a feedback loop, either via a proportional integral (PI) or proportional integral derivative (PID) controller. First a reference signal is generated and cross referenced against the cantilever deflection. From this the gain is tweaked to attempt to apply a constant force to the tip across measurements (setpoint).

From this loop, the tip position and the cantilever deflection is recorded. This loop helps to ensure that a constant force is applied to the tip, to reduce tip and sample damage as well as the reduction of errors in the system. [16][1]

Elaborate on PID controllers and feedback loop futher?

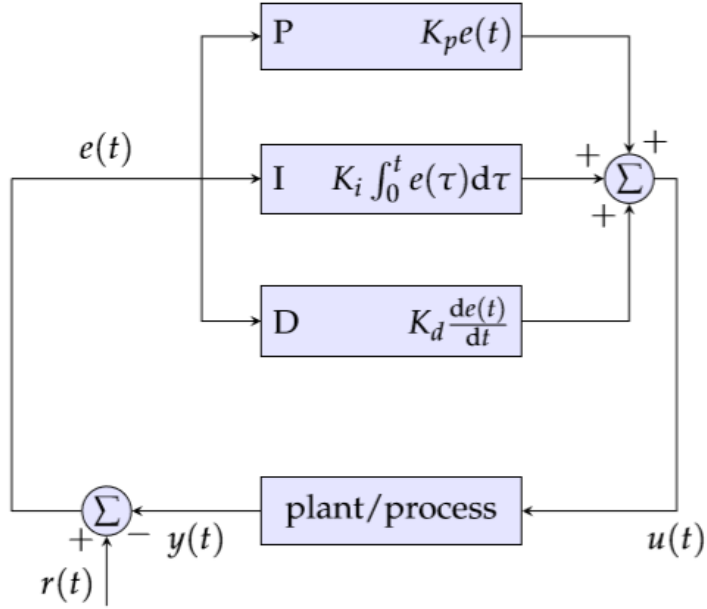


Figure 2.3 A basic schematic of an PID-controller circuit where $r(t)$ is the setpoint, $y(t)$ is the reference signal and $u(t)$ is the difference. P calculates the weight of the error signal input, I weights the sum of previous errors and D calculates the change in error over time to predict future errors. Image adapted from [16].

Using this loop the tip can then be exposed to various ranges, with corresponding forces acting upon it. These ranges are known as contact code, where the tip comes into full contact with the surface, tapping mode, where the tip only lightly grazes the surface and non contact mode, where the tip is only affected by the long range repulsion forces. As you move the tip further away from the surface the force applied on the surface is reduced, which is particularly useful for softer samples. For force curves however, the force measured is generally across the spectrum. [16][1]

2.3 Imaging mode AFM

Imaging mode is a type of AFM operation which measures the z-height of a sample across a x,y scan range. The positions are recorded in a three dimensional array, with the distance between each x,y point being constant. The major operation is much the same as described above, with the difference of a pizeo controlling x,y movement in addition to z-peizo. The surface of the sample is imaged across using a raster pattern. This array is then converted mathematically into a heatmap.

The AFM used for imaging was the Bruker Nanoscope 2, which contains a sample

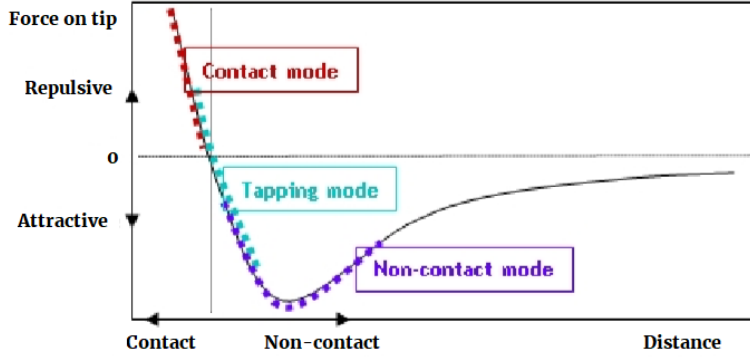


Figure 2.4 A Van-der-Waals potential with corresponding regions of contact imposed over the curve to demonstrate the ranges each of the modes have in relation to the forces applied to the cantilever. Image adapted from [16].

mounted on a 1cm disc, atop the J scanner piezo. The head unit is then held down using springs, and a mirror used to align the laser onto the mounted cantilever.

Some AFM setups also provide other images during scanning; a phase image, an amplitude (Or deflection) image and a friction image depending on what operational mode the AFM is set to. Generally two operational modes are available for the operator; contact and non-contact mode. Contact mode physically brings the tip in contact with the surface, then drags it across the surface. This is useful for measuring friction, reducing current effects on the tip in a liquid AFM situation and physically interacting with surface objects on the nanoscale. Non-contact mode oscillates the cantilever above the surface, only allowing the tip to touch the surface gently at the nadir of the oscillation. By subtracting the input oscillation from the physical oscillation of the cantilever the phase can be determined. This indicates the softness of a surface, as harder surfaces dampen the movement to a greater degree, reducing the angle of the reflected laser.

2.4 Tip Calibration

Tuning a cantilever for use under imaging mode is generally simpler compared to force AFM. By sweeping a cantilever over a range of drive frequencies a maximum peak of cantilever amplitude can be found. From this the resonance frequency is assumed. However issues can arise when calibrating a tip for use under liquid.

Sader method?

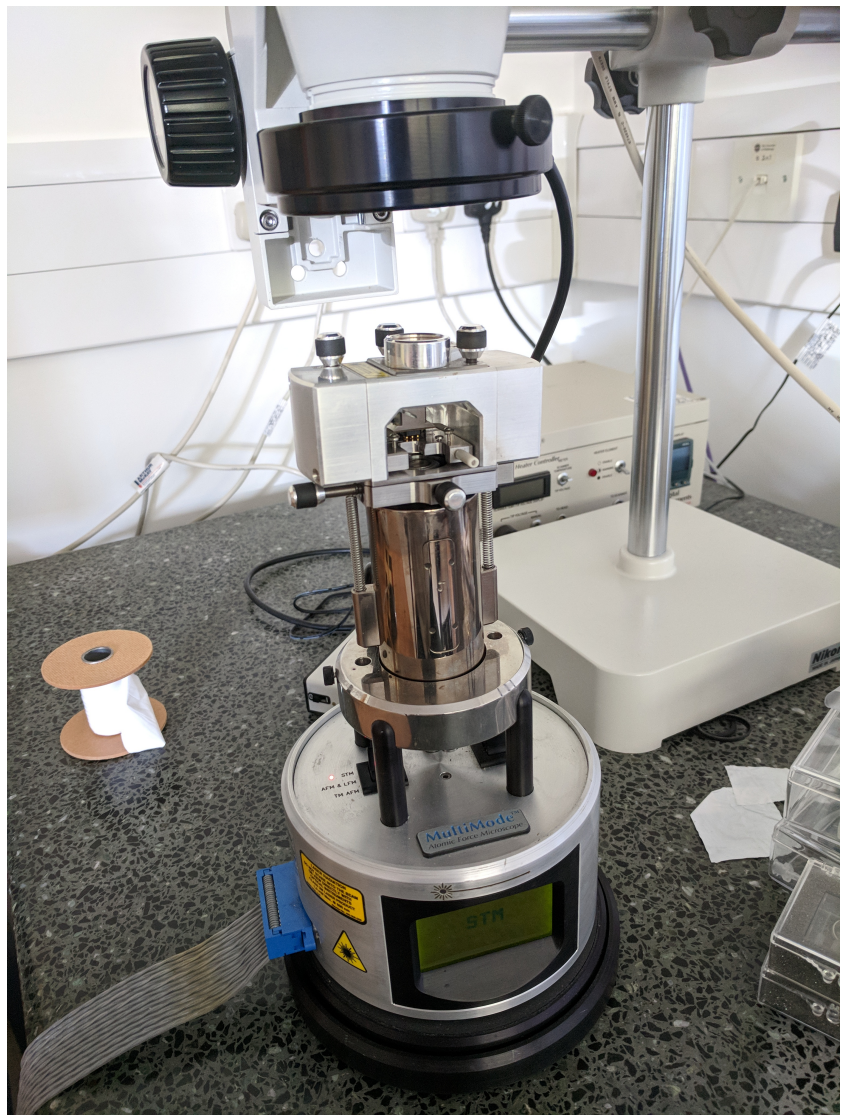


Figure 2.5 *Photograph of the operational setup for the Bruker Nanoscope 2, which was used for image measurements.*

2.5 Mathematical alignment and error

The use of AFM has proliferated across the sciences due to its wide range of applications and data output, however in some cases the image produced is assumed to perfectly reflect the surface of the sample, when in reality there are a number of mathematical, physical and operational effects that can vastly affect the output image. Mathematical transformations are applied to the raw data via image processing. Physical errors can occur from the situations the tip is exposed to and the condition of the tip. Finally operational errors can occur from improper use. As a result it is important to consider where errors can arise to ensure that the image produced from the machine is a reflection of the true surface of the sample.

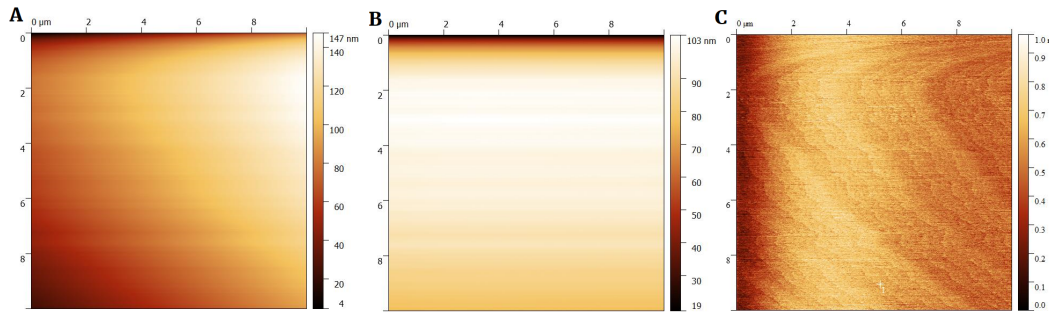


Figure 2.6 A figure demonstrating a standard mathematical operation applied to raw data. A demonstrates the array shown direct without any processing, B has had a mean field plane subtraction applied and C has had row alignment applied to it. The image itself is of a freshly cleaved mica surface.

Mathematical operations are performed on all images as the data generated does not account for the tilt of the surface, therefore a degree of mathematical transformation is required. Initially a heatmap of the the output will look similar to Figure 2.6. A mean field plane subtraction is used to determine the plane on which the data was generated, then removed. This is to provide the raw height data on a theoretical flat plane. Next the rows of data are aligned by taking the representative height of each row and aligning each row to that height, this is done by several different methods, such as polynomial or median methods. As a result the features on the surface of a sample are kept intact, but it is possible that sharp differences observed on a row by row basis can be obfuscated due to image processing. The size of a pixel is dependant on the scan size (for example a 10um by 10um image with 512 data points per line means that each pixel is approximately worth 20nm). In order to reduce errors like these and to resolve features that may be hidden by pixel weight larger scan sizes are often coupled with smaller scan sizes to give both the larger order topography with the smaller detail analysis. It is important for an user to not perform too much image processing without explanation and reasoning as each additional step is a further abstraction from the truth.

Another consideration with AFM is that since the image is scanned over time rather than instantly there is a degree of physical error introduced during operation. Thermal fluctuations, piezo-error, vibrations and air fluctuations. Generally the error of an AFM in imaging mode is given to be +/- 1 nm on the x and y length scale and +/- 1 angstrom on the z length scale. Issues are made worse within liquid conditions where current effects induced by probe movement, vibrations, sample setup and approaching the surface can frustrate results. The change in refractive index in the liquid means that the laser has to be realigned and re-calibrated in more difficult conditions. Additionally it is important to assess images produced for unusual mechanical errors, such as the double tip effect, where the tip becomes damaged during scanning and the defect in the tip's geometry is reflected onto a sample. There runs the risk of papers

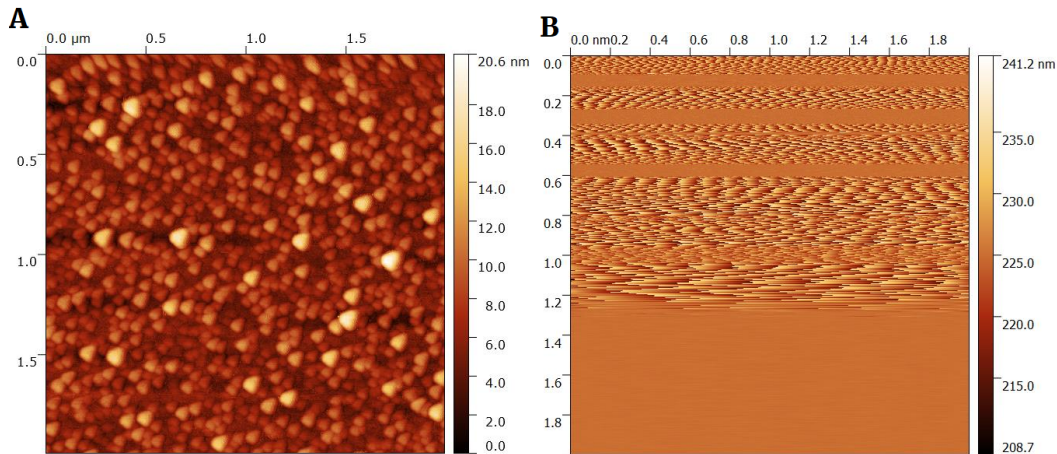


Figure 2.7 A figure demonstrating different errors and operations on the output images produced from an AFM. A. demonstrates a physical complications known as the double tip effect produced by tip damage. B. highlights an example of the zigzag patterns that can be produced from operation error, as well as the blank areas where the tip is not in contact with the surface.

being published with potential double tip effects within their AFM analysis to an unknowing operator, the double tip effect is shown in Figure 2.7.A.

The operator is able to adjust several variables whilst operating an AFM. How much force is exerted on the surface as a result of the tip's proximity is altered, too light and the output image is unclear, but increasing force causes increased tip degradation rate. The scan rate is how fast the AFM scans, faster speeds increase image production, reducing the effects of drift, piezo error and thermal fluctuations, but a high scan rate can result in unclear images and an increase in tip degradation. Finally gain can be adjusted, the values of which vary on the sample, setup and device. Images produced with incorrect settings can result in wavy mechanical patterns or poor image quality. An example of a tip that hasn't engaged the surface properly, therefore resulting in a poor pattern is shown in Figure 2.7.B. [5, 40]

2.6 Force microscopy

Force microscopy operation of an AFM differs from imaging mode in that the x,y movement of the piezo is removed, and instead a static sample is placed underneath, with several curves taken of a single site.

2.7 Tip calibration

After the laser has been aligned the system can detect changes in the cantilever, in particular bending. However, for this bending to be converted into force applied to the cantilever, the cantilever itself must be calibrated. Unlike imaging mode where the peak resonance is the main factor in calibration, the spring constant is calculated using a thermal power spectral density graph coupled with the inverse optical lever sensitivity (InvOLS). This is due to the force being calculated, rather than imaging producing a heatmap based off the cantilever deflection. In the case of force;

$$F = kz \quad (2.1)$$

where k is the spring constant of the cantilever and z is the cantilever deflection. The cantilever deflection is in turn calculated using:

$$z = In_{vols}\Delta V \quad (2.2)$$

Where In_{vols} is InvOLS, and V is the change in the voltage measured by the photodiode. V is given as a raw value from the machine.

InvOLS can be calculated by taking the slope of the curve on a hard surface, then finding the difference needed to convert said slope to be equal to one (Figure 2.8. Not certain on this, reading the IGOR code seemed to indicate this was the case

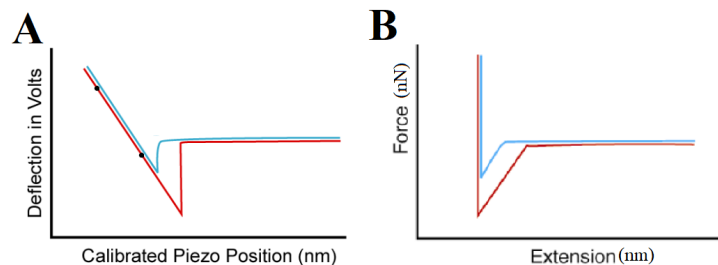


Figure 2.8 A diagram demonstrating the effects of calculating the InvOLS, A demonstrates the raw data plotted, B demonstrates the data adjusted with InvOLS Adapted from [26]

The spring constant of the cantilever is calculated using:

$$\frac{1}{2}k_B T = \frac{1}{2}kx^2 \quad (2.3)$$

Which can be simplified to:

$$k = \frac{K_B T}{\langle x^2 \rangle} \quad (2.4)$$

where K_B is Boltzmann's constant ($1.38064852 \cdot 10^{-23} \text{ m}^2 \text{ kg s}^{-2} \text{ K}^{-1}$) and T is temperature in Kelvin. x^2 is distance in respect to the power spectral density (PSD), which is fit to a simple harmonic oscillator. [6, 25]

Add review here.

2.8 Application of Derjaguin approximation

Chapter 3

Surface Imaging

3.1 Introduction

In order to characterise the borosilicate glass capillaries used an Atomic force microscopy (AFM) investigation was performed. This intended to investigate the uniformity of a borosilicate capillary across multiple capillaries by profiling the surface topology and roughness within the same length scale of the cantilever heads. This glass capillary was then cross referenced against the petri dish in use, to ensure that the surface of the petri dish was representative of borosilicate glass. This surface was then referenced against scanning electron microscopy images of the tips, alongside inverted AFM imaging of the tip.

Initially the inside of a glass capillary was imaged.

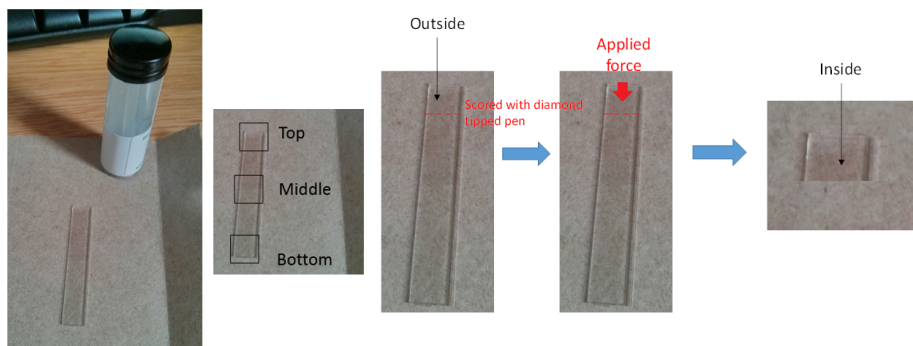


Figure 3.1 A diagram demonstrating how the glass capillary was broken and how samples were extracted from the capillary.

The inside of the capillary was imaged by scoring the glass with a diamond tipped pen, with pressure applied on the outside to break the glass cleanly open 3.1.

The sample was then loaded inside up into a Nanoscope AFM under tapping mode operation in air. Multiple antimony doped silicon tips were used to scan

several samples each, giving a range of tips used for imaging. This was done to reduce any tip artifacts or degradation of tips so that image quality was retained throughout. A constant scan rate of 0.4Hz across all samples with the integral and proportional gain determined using the initial sample, then kept constant at 0.22 and 0.63 respectively. This was done to produce images that were similar as possible to one another from a parameter point of view. Each capillary was imaged 12 times at a 10m x 10m scan size followed by a 2m x 2m scan size. Images were taken at the top, the middle and the bottom of the capillary with a repeat image taken per site. Finally, two capillaries were imaged giving a total of 24 images. Scan sizes were chosen to give a larger view of the surface of the capillary giving respect to the initial size of the silica bead on the end of the cantilever chosen for use with the surface profiling methodology (1.6m x 1.6m). Resultant images were then mean plane subtracted to remove image tilt, with each row aligned afterwards using a 5th order polynomial transformation. The images were then saved and compared by eye. Any images with objects identified as dust were then repeated to ensure that said object was dust and to provide a clear image of the surface topology.

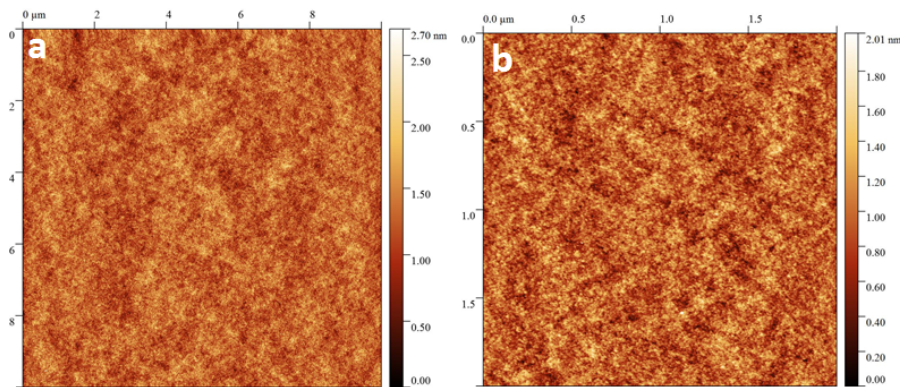


Figure 3.2 Two sample AFM images of untreated borosilicate glass at two different scan sizes: (a) displays an image with a scan size of 10 μ m x 10 μ m, while (b) demonstrates a scan size of 2m x 2m.

The images produced showed a uniform surface across the 24 image dataset, with a maximum peak to peak roughness of 3.64nm for 10m x 10m images and 2.55nm for 2m x 2m images. Figure 3.2 demonstrates an example of each image per scan size, giving the general topology of the observed glass. The observed images demonstrated that the topology and roughness of the capillary was constant across the entire length of the inside capillary as well as uniform across multiple capillaries. As a result of these images the capillaries used in the main investigation are assumed to demonstrate similar surface structure to figure 3.2.

In order to ensure that any error incurred by physical error was accounted for an investigation into the x, y and z error was carried out. The AFM was left to image the same glass sample repeatedly in order to produce the same image

several times. This image was then two dimensionally cross correlated with the next image in the sequence and the difference removed between the two z data points. The results are displayed in Figure 3.3.

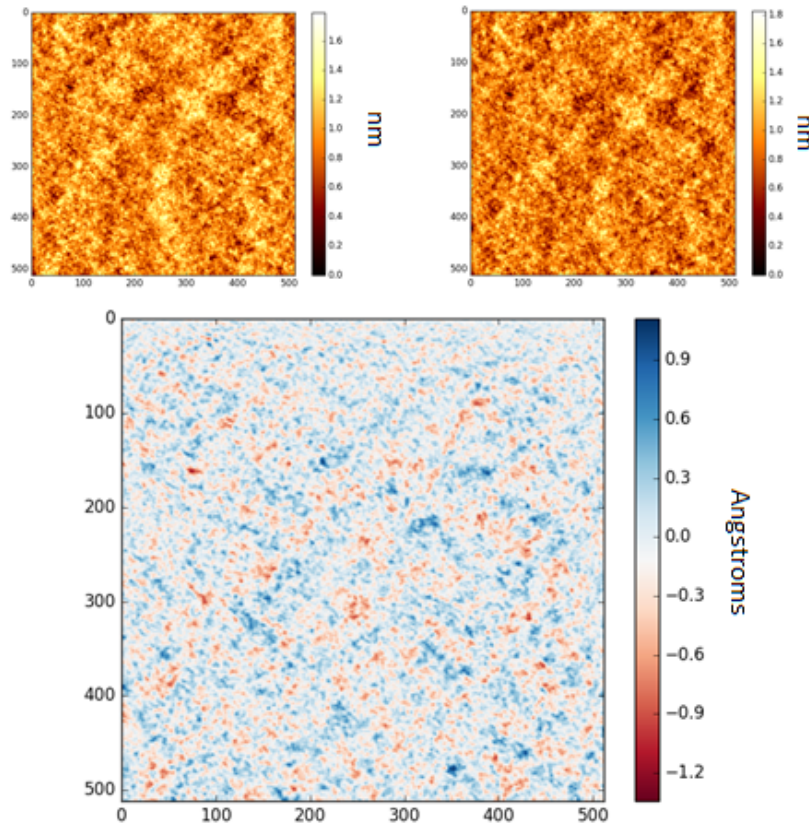


Figure 3.3 The output image of the 2D cross correlation function between the two images. The two smaller images are the input images into the script. The x and y values are the location of the z values in the 2D matrix dataset. The z scale is labeled respectively.

Due to the drift experienced while scanning, the rows were found to be increasingly misaligned towards the bottom of the image. The result of this is shown by the gradient seen from the top of the image downwards, as the first image scanned from the bottom up, then the second image was scanned from the top down. The process was repeated on a row by row alignment basis and the resultant drift between the two images was found to be approximately 1 angstrom on the z axis, 8nm on the y axis and 28 on the x axis. However given the speed of the scan was low at 0.4Hz each image took approximately 40 minutes to image, giving an approximate drift of 0.1nm by 0.5nm drift per minute.

3.2 Silica particle surface resolution

Successful resolution of a $1.5\mu\text{m}$ silica sphere was imaged under AFM and spherical deconvolution was processed with gwyddion. [28] Further work will be done to investigate adhesive forces between silica particles and to determine if the "pit" present in the center of the image is due to sonication.

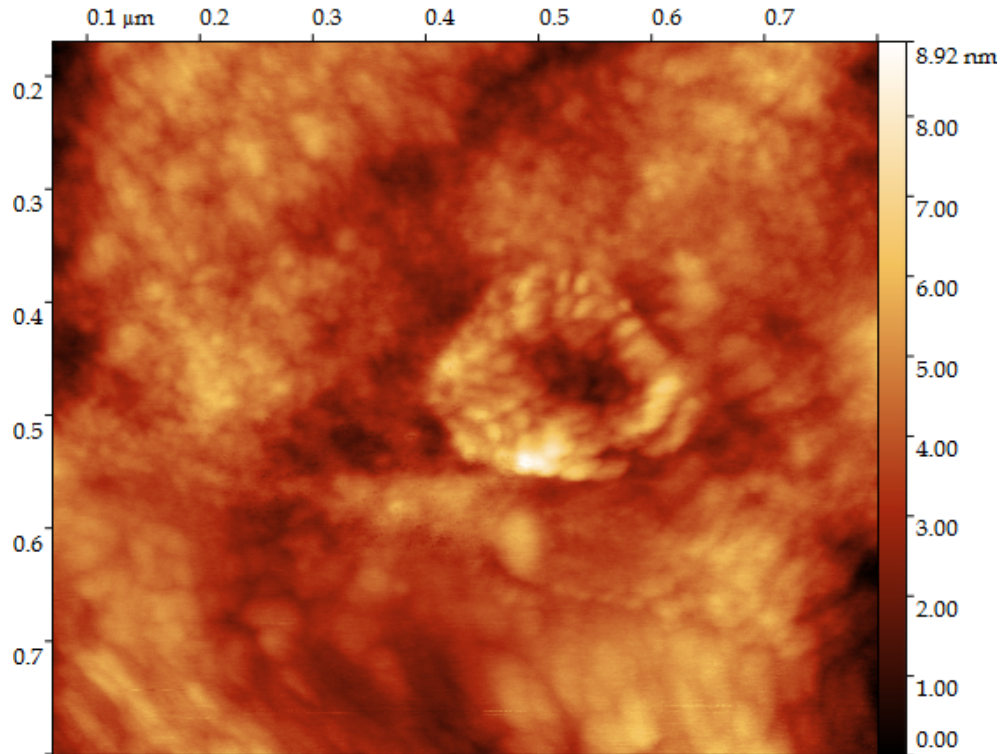


Figure 3.4 The flattened surface of a silica sphere.

From the region any tilt or shift in the constant phase is taken away from the whole dataset.

3.3 Root mean squared roughness

Chapter 4

Atomic force spectroscopy analysis

4.1 Introduction

This chapter explains the experimental methods used for force curve collection as well as the computational methods used to interpret them. Over the course of data collection the process was refined to a repeatable method across a consistent experimental setup. While two different AFMs were used across the analysis, encouraged by technical limitations, they were used in such a way to complement one another. Both of these AFMs were used to produce force curves, and were interpreted using the same scripts.

4.2 MFP-1D

For the force microscopy setup a MFP-1D from Asylum Research was used. The MFP-1D is an AFM mounted on top of an inverted light microscope, with the sample placed between the scanning head and the stage of the light microscope. In the AFM head the cantilever is mounted using tweezers in a holding apparatus. This head is immobile in the X,Y direction, horizontal movement is instead controlled by manipulation of the stage. In the Z direction there are two possible movements - the 3 legs of the head can be moved vertically using the wheels for coarse movement, either to bring the tip in contact with the sample, or to level the head so the contact of the tip with the surface is uniform. The other control over the vertical height is via the piezoelectric transducer (piezo) mounted in the center of the head. This piezo has a travel range of roughly 15 μm . A laser is then emitted from inside the head and directed onto the cantilever, towards the sample. (See fig 4.1)

For laser alignment on the AFM head an inverted microscope is used. First the cantilever is brought into focus under the microscope, then the position of the

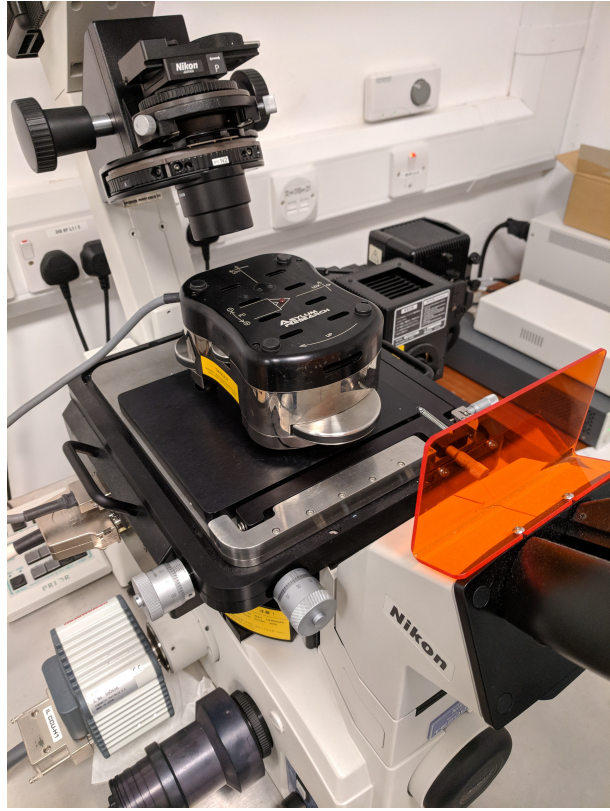


Figure 4.1 Operation setup for the MFP-1D AFM that was used for force measurements.

laser is aligned atop of the intended cantilever. Afterwards the laser is focused upon the center of the tip using the sum output given by the photosensitive diode. The diode converts photonic incident light into an output voltage, this allows the position of the laser focal point to be determined with respect to the diode boundaries. Finally the deflection of the laser is set to 0; a central position between the positive and negative extremes. deviation of the laser's focal point from the center point of the photodiode allow movements of the cantilever to be detected. This detect any bending (and thus attraction/repulsion) of the cantilever.

In terms of the structure of the device, it differs slightly to the imaging AFM explained in the previous chapter; the components are more tightly packed, mounted atop of the z-piezo directly, which then brings the apparatus down onto the sample, unlike the z-piezo raising the sample up to be imaged. In addition a linear variable differential transformer (LVDT) sensor is mounted inside of the head to correct the movement of the z-piezo (closed-loop piezo) thus improving z-piezo accuracy (See fig 4.2).

Due to this feedback loop from the LVDT relying on previous data to define the voltage control from the next approach, the peak force (the intended maximum force applied on the cantilever per curve) was set to a relatively low number 8

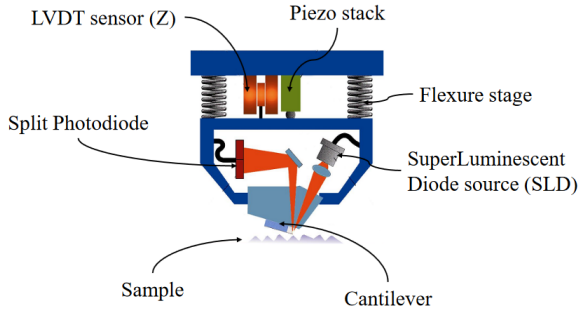


Figure 4.2 Operational setup for the MFP-1D AFM that was used for force measurements. Adapted from [26]

nN. This was done to limit the amount of tip damage during operation. In cases where the tip fails to engage with the surface in the previous approach, this low peak force ensured re-engagement of the tip with the surface in the current loop was as gentle as possible. Noise in the data was attributable to the effect of vibrations on the operation of the instrument. When errant vibrations reach the AFM, this energy is transferred through to the cantilever, which then causes it to oscillate. This oscillation usually presents itself as a sudden spike in deflection on the curve. It is these sorts of curves that are selected and removed from the dataset. In most cases the total amount of removed curves is minimal, usually 1 or 2 per site, with a total of 100 or more curves used for processing. While it was rare that any datasets were rejected for purely noise based reasons, there is one notable set that was repeated at a later date due to Storm Emma causing significant, persistent errors in the data.

Additionally, the standard speed of tip movement was set to 1 $\mu\text{m}/\text{s}$ (unless otherwise stated). This was done to compromise between the total dataset recording time and reduction of strain upon the cantilever and tip.

4.2.1 Experimental setup

Initially the experimental setup was focused on investigating the interactions between two silica particles. Given the difficulty in aligning two micron sized particles for interaction, the first experimental setup involved using a silica particle glued to a cantilever (see fig 4.3). These types of cantilevers are produced commercially, and were purchased to reduce experimental setup time. This cantilever was then brought into contact with a silica surface, with the results transformed using the Derjaguin approximation (See chapter 1).

The first setup involved a 1.6 μm diameter tip brought into contact with a silica surface glued to the inside of a plastic petri dish. This setup allowed for a liquid solution to be placed on top of the surface, contained within the plastic petri dish. A 50:50 solution of deionised water and glycerol with a controlled concentration

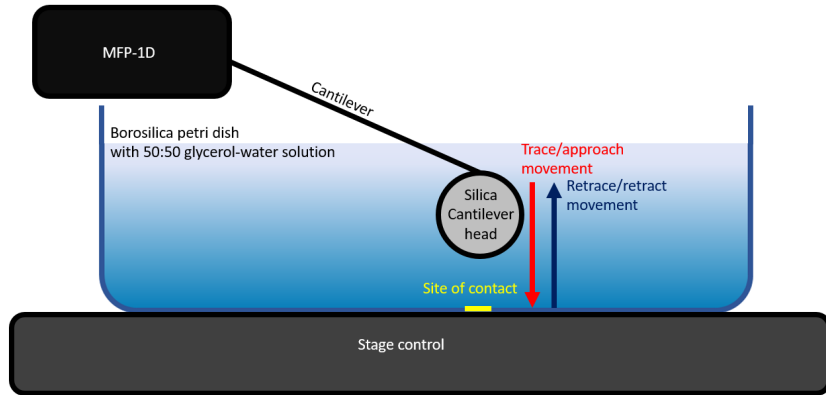


Figure 4.3 Experimental schematic of MFP-1D during operation. The AFM is abstracted away into a back box to highlight the motion that the cantilever takes with respect to the surface. The stage control provides horizontal control, and therefore moves the projected site of contact along the petri dish surface.

of LiCl was added. This solution was brought up to completely cover the tip, and ensure the head of the AFM was submerged.

The initial setup involved calibrating the cantilever tip on a separate calibration surface (see chapter 2), then removing this surface and replacing it with the experimental one. Initially approaching the surface was of little issue, but the greatest difficulty arose in finding contact with the surface under liquid. Given that the liquid in use was of a different optical density than air, the interface between the two was no longer visible under the microscope. As a result; the initial approach was slow, methodical and careful, as recklessness would break the tip.

Problems with the setup were identified after a test run, after a sweep of 4 different concentrations it was found that the resulting Debye lengths for all the curves were above 6 nm. These were directly contrary to the expectation that Debye length should decrease to theoretically 0 at increasing salt concentrations. The anomalous readings were considered to be the result of unidentified contaminants. Given the setup with the AFM was open by necessity as well as the difficulty in getting the sample under the tip in an expedient manner, there was little protection against airborne contaminants. Equally contaminants originating from the plastic of the petri dish and glue were identified as a source of problems. The method of cleaning the surface was also called into question.

In order to address these issues, a few changes were implemented over a series of experiments. The surface used was exposed to an improved washing protocol. This washing protocol used deionised water to clean the surface over a greater period of time. Ethanol was considered, but due to the glue holding the surface down, there were concerns over the surface having a stable platform. Additionally the method of approach was revised slightly, with a large part of the distance

between the surface and the tip performed in air, with the liquid solution injected using a glass pipette slowly. This injection relied on the surface tension of the water to slowly fill the dish, resulting in a slightly higher volume use. This was done to minimize any dramatic flow from damaging the tip, emulating a normal approach submerging mechanics.

Contamination issues were still present after these revisions. In order to maximise contaminant removal, the plastic petri dish was replaced with a borosilica glass one. Instead of gluing a surface on top of the petri dish, the surface of the dish itself became the sampled area. While there had been previous considerations of the stability of the glue influencing the resulting force curve, the approach had been focused on solving the contaminant problem first. By using the surface of the dish itself, any concerns regarding glue induced artifacts could be laid to rest. This new dish permitted the use of ethanol in the cleaning procedure, as well as plasma treatment of the surface. The silica bead diameter on the cantilever was also increased to $6\text{ }\mu\text{m}$ to increase the area of contact.

Plasma cleaning was performed under a vacuum within a sealed chamber. After the chamber was evacuated a low quantity of pure oxygen gas is flowed across the surface at 0.4 bar, with the vacuum pump still active. This plasma cleaning technique cleans off any residual organic matter, resulting in water and carbon dioxide byproducts. These byproducts are pumped away by the constant vacuum. [31] [45] [3]

The final protocol that was used is as follows: The glass petri dish and lid was cleaned with ethanol and water, followed by plasma treated. The lid was replaced immediately after, and remained on until use. The cantilever was mounted into the AFM head, and the laser aligned as closely as possible to the center on the photodiode. The petri dish was then put under the head, and its blank surface was used to calibrate and calculate the spring constant of the cantilever. The cantilever was then retracted by a known amount, and then the liquid solution was the pipetted in. After the liquid had settled, the laser was recentered to adjust for the change in optical density. The tip was then brought into contact with the utmost care, relying on deflection readouts due to blind nature of the approach. Finally after contact, 100-200 curves were taken per site. If multiple sites were taken, the tip was retracted slowly, the petri dish moved slightly, and the approach phase was repeated. When transition between differing electrolyte concentrations, the tip is retracted, cleaned carefully with water, and plasma treated along with the petri dish. Otherwise the protocol was repeated. A tip was not plasma treated more than twice due to the degradation of the tip (see fig 4.4).

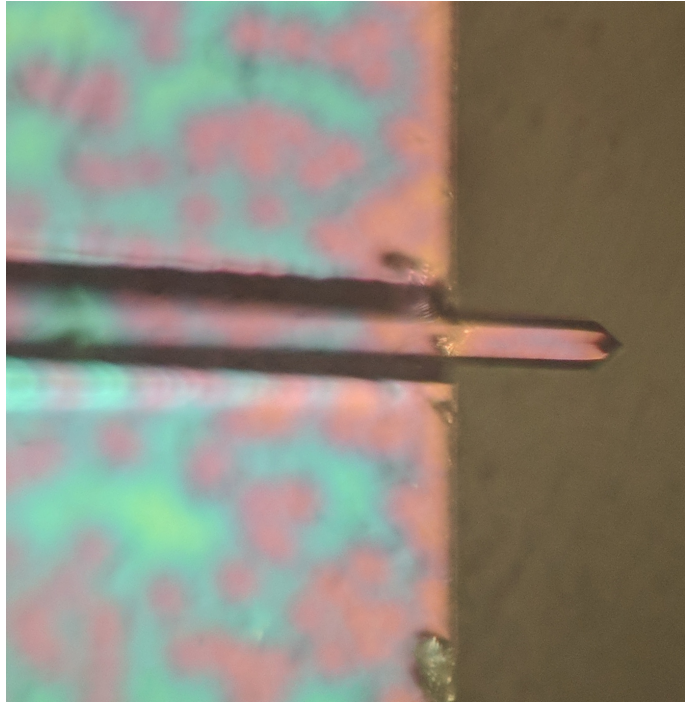


Figure 4.4 The view of a tip overtreated by plasma down the viewport of a microscope. Normally a tip is silver on the outside, but from over-treatment the surface has worn away.

4.2.2 MFP-1D force-distance curves acquisition and processing

Acquisition

For each measurement site, a minimum of 100 force curve readings per site was taken, with the raw data saved in a single file. The columns alternated with the raw deflection reading for one curve, followed by the corresponding z-piezo value. For the majority of readings the whole curve is measured throughout the reading, combining the approach and retract curves into one whole column. In the case where the cantilever is held at a certain location for a period of time, a new set of columns is appended, with another one starting after it begins movement again, thus fracturing the data whenever the cantilever is stationary between periods.

From this each curve was broken down into two lists of raw unprocessed data given from the machine; the piezo height and the deflection. The piezo height is the recorded height of the cantilever on a scale of 0 μm to 6 μm . This range corresponds to the effective movement of the piezo in the z direction, and is thus variable between datasets, as contact can be anywhere within this range. It is worth noting that the z height controlled by the legs of the AFM is independent, and is not measured by the machine. Contact is a combination of the leg height being set by the operator manually, and the piezo coming into contact

within its 15 μm range. The cantilever deflection is the deviation in nm from the equilibrium position, which corresponds approximately to the center of the photodiode. Deviation from the center arises from when the cantilever is bent in a certain direction, reflecting laser off the top of the cantilever to drift along the photodiode's sensory range. This voltage is recorded as either a positive or negative voltage corresponding to upwards or downwards deflection due to repulsive or attractive forces, respectively. This deflection is saved alongside the height in individual data files during operation automatically, with any derivative graphs following the same naming convention defined by the input file, with respect to unpacked bulk site curve set.

In some cases the resultant curve is not typical. This can arise when the cantilever doesn't move far enough down to find the surface, or when the cantilever starts in contact with the surface at the start of the movement. While these curves were rare, they did occur during standard use of the AFM. These curves were removed during processing. These erroneous movements were usually corrected automatically by the AFM via error correction feedback for the successive curves afterwards. In some cases, due to imperfections of the control mechanism of the AFM, tremors/ vibrations in the building or other uncontrollable factors the frame of reference can shift up, resulting in an unusable curve, simply due to the lack of a data in a specific area. These fluctuations in the system cause the AFM to "lose" track of the surface and command an increase to the voltage sent to the piezo, over-correcting its movement, shifting the captured area further up. After this the error correction it reduces the voltage until it stabilises. In addition, in the case of an uncontrollable error (primarily vibration based) the noise of a specific curve can throw off the normal processing of the script. It is in these instances that these curves are identified and removed.

Using python[37], an automated was script constructed to process the large volume of data generated by the MFP-1D AFM, given that each site generated around 100-200 approach and retract curves, and that multiple sites were used for each concentration, this produced a sizeable volume of data of around 6,000 curves which would be unmanageable without some form of automation.

Processing

Using numpy[30] an array was set up from the data present in the raw data file for a specific site. Each of the curves for a given site is then split up into individual numpy arrays in preparation for the following functions. As it stands, this raw data requires at the bare minimum translation from a distance vs distance graph into a force vs distance graph. This corresponding graph is produced of force (nN)vs z-piezo position (μm). The raw deflection is converted into force (nN) using the spring constant of the cantilever with the following equation[7].

$$F = K_c(\delta - \delta_{offset}) \quad (4.1)$$

Where F is force, K_c is the spring constant, δ is the deflection and δ_{offset} is the deviation intrinsic to the cantilever under no force.

Equally the z-piezo position is converted into nanometers (See fig 4.5). This produces both an individual data file for ease of use on repeats, as several runs are expected to hone the parameters down to improve the quality of the analysis.

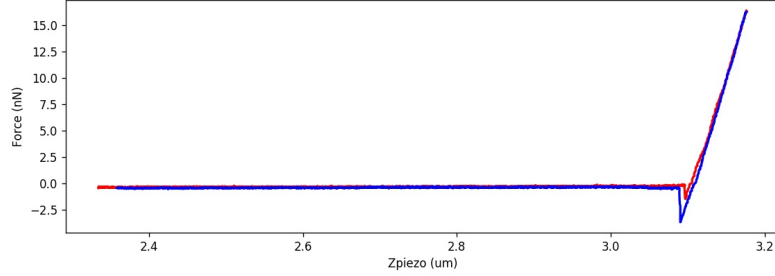


Figure 4.5 An example of a individual graph produced at this point. Minimal processing has been done with only the deflection converted into force (m to nN) and piezo z position m into μm

In order for the script to perform correctly on each of the curves, there needs to be a long enough stretch of data for the approach, and equally a long enough contact region. In the vast majority of cases this is true, there are a few cases where during normal operation an over correction occurs, resulting in the frame of reference to be shifted along the theoretical master curve. The operation parameters of the AFM aim to collect the most amount of data around the inflection point while reducing the amount of unneeded movement towards the surface, and equally reducing the amount of strain forced upon the cantilever during the contact region. At high strains the surface of the cantilever or petri dish can become damaged, or the cantilever can become damaged or break. As the conversion of deflection into force requires the spring constant to remain the same, and damage can cause this conversion to no longer remain true, any damage over the operation is considered by reviewing the curves over time. If there is a significant drift in the shape of the curve over the process of a site, then this is highlighted, and experiment repeated. In the event of the cantilever breaking the AFM ceases to function, and therefore data collection stops.

Each curve is then processed individually. The first step taken is to address some of the background noise, this is done by taking a linear portion of the curve (see fig 4.6), where any movement done by the piezo is far enough away that any forces acting between the surface and the cantilever are zero. This removes any farfield drift, intending to remove any gradient found along the linear non-contact region.

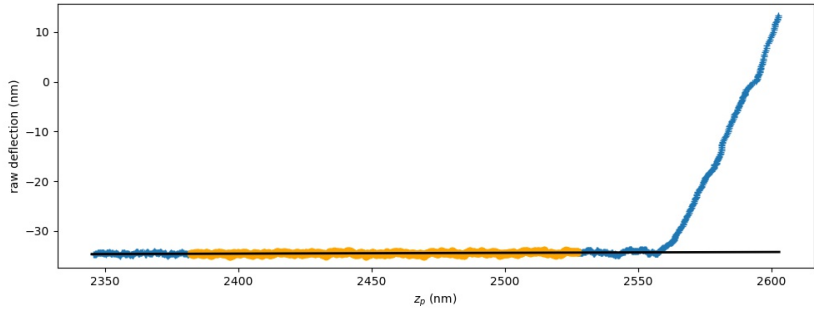


Figure 4.6 An example of a individual graph produced for a single approach curve. The orange region of the graph is the area used in the farfield drift reduction and used to set the floor of the data to 0.

This area is defined by a region along this curve, set to use points away from the initial contact area of the curve. Initially the distance traveled per datapoint is calculated by taking the adjusted range of data divided by the total number of datapoints. From a combination of user input and estimating where the contact area is, and working backwards, the data window is set along this linear regime, with a respective graph produced to indicate what region is selected. This linear region is then floored, with the whole dataset translated up or down to the point where the region is at 0.

Afterwards the data is binned into a set of variable size. The size of this set is determined by trial and error on a per case basis, in most cases the bin size was 5. In earlier curves where the total number of data points taken was 2000 per curve, the bin size was smaller. Subsequently the size of the data collected improve the resolution and this improve the data analysis. Afterwards it was determined that increasing the total number of data points to 8000. The objective of this set was to produce a smoother curve and reduce the effects of noise intrinsic to the system. Smoothing the curve in this manner improves the accuracy in which the contact point is defined. A graph is additionally produced with a bin size sweep of ± 2 to ensure that any features were not lost during binning.

After binning, a first degree polynomial is fitted to the selected data. In the case where a suitable fit could not be found for the curve, this set is skipped, and the curve is left untranslated.

Once binning was complete attention was given to the selection of the data which best represents the area in which the tip has made contact with the surface, where any peizo movement was translated into cantilever deformation. In general, this selection was defined by reviewing the graphical output from the previous steps (see fig 4.7). This selection aims to include as much as the graph as possible after the contact point, though it should be highlighted that the material in the cantilever is not uniform and therefore deformation is not a purely linear event in practice. In order to ensure that the contact region is within a local minima, the upper and lower boundaries of the range sweep ± 5 arbitrary units. From

this a final graph of force at contact is produced.

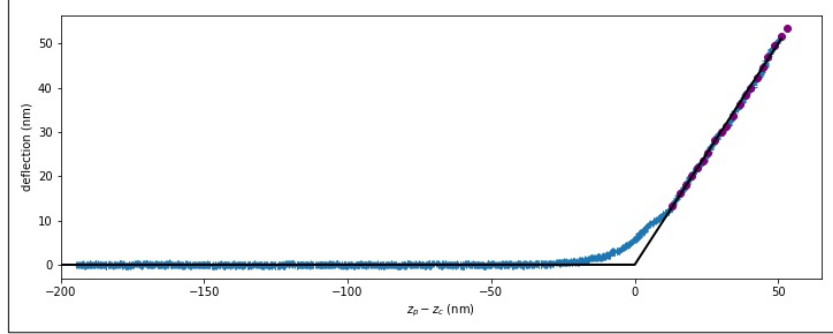


Figure 4.7 An example plot of an approach curve. The area used to define contact is highlighted by the purple dots overlaying the raw curve.

Using this defined region, the data is extrapolated back to the intercept. In the case that there is a jump to contact, the jump point is used instead of the interpolated z_c . Where the extrapolation intercepts the floor line is where z_c is defined. Each curve is then normalised to 0 using z-piezo position (z_p) minus z-piezo contact point (z_c) at the point of contact. This term is defined at z-peizo separation (z_{sep}). In conceptual terms where $z_{sep} = 0$ is the point in which the cantilever would come into contact with the surface under no outside stress.

$$z_{sep} = z_p - z_c \quad (4.2)$$

In the case where some individual curves have a high range of forces/deflection (usually as a result of overcompensating) this region of the graph is removed. This is because of the non-linear region intrinsic to the photodiode detector. Care is taken to ensure that the analysis is done within the linear response region of the photodiode. This region is where the laser reaches the limits of the photovoltaic cells and the overall signal strength is reduced. Additionally, at higher stresses cantilever deformation can result in non linear deformation. As the system itself assumes a constant, these can cause abnormal data points at the end of the curve. It is in these circumstances, where the behaviour of the curve is inconsistent with the known behaviour of the machine, that the data is removed.

In order to ensure that the region defined by the operator is correct, a number of diagnostic graphs were produced in order to aid the selection process. The gradient of the deflection is calculated with respect to the stage height in order to highlight the transition between the movement phase and the contact phase of the graph. This is done for individual curves as well as an averaged curve (see 4.8).

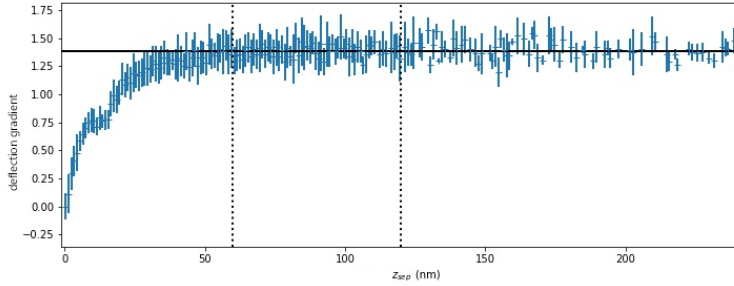


Figure 4.8 An example plot of the averaged approach gradient. This graph focuses specifically on the region after contact and The area used to define contact is highlighted by vertical dotted black lines. The horizontal black line indicates the extrapolation of the data. in this case the data is binned to reduce noise. The height of each blue bar indicates the standard deviation for each point.

These curves are then all plotted on top of one another to check that all curves follow the same rough shape (see fig 4.9).

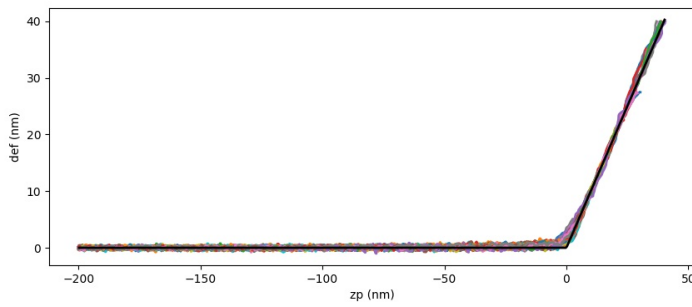


Figure 4.9 An example plot of all the curves for a given site processed up until this point. A reference black line is overlaid demonstrating what a curve would look like with only terminal electrostatic repulsion.

This resolves in a final averaged and binned force curve (see fig 4.10)

Afterwards the focus of the script changes to calculating the force applied at contact. Positive forces indicate a repulsive force, negative forces indicate an attractive force. A Savitzky–Golay filter is applied to the data to reduce the noise intrinsic to the data. [34] Then the curve is followed algorithmically until it passes over the threshold point - by default where separation is 0.

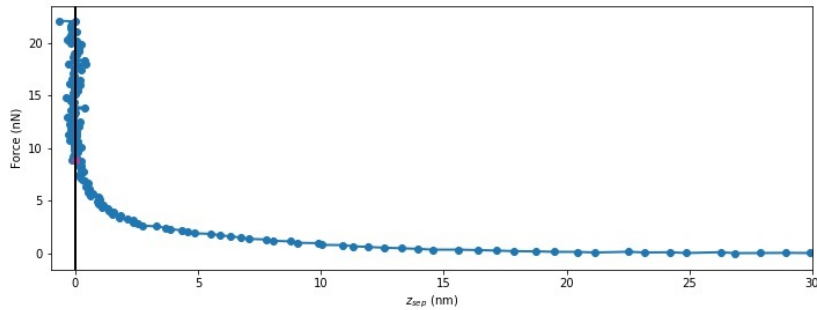


Figure 4.10 An example plot of the final processed force curve. The y axis has been translated to show the distance from contact, with a black line highlighting the defined point of contact. The datapoint used to define the force at contact is highlighted in red.

This is done for each individual curve, eventually resulting in a histogram of contact forces (see fig 4.11).

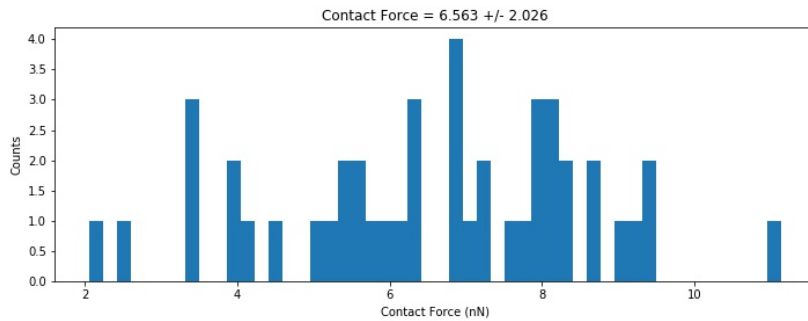


Figure 4.11 An example of a histogram produced from a set of curves for specific site. The mean force is given at the top with the standard deviation.

In most cases the total number of individual graphs per final force datapoint is between 80-200 curves.

4.2.3 Validation of results

In order to validate that the data produced by the procedure met the precedence set by theory, the Debye length was experimentally determined. This approximation of the Debye length (κ) was calculated using the equation outlined in chapter 1 (see eqn ??). The experimentally calculated value was then checked against the approximated Debye length across a sweep of concentrations. This was in part to ensure that the procedure gave sensible results as well as a means of detecting invisible sources of contamination.

This procedure produced sensible Debye length measurements according to the

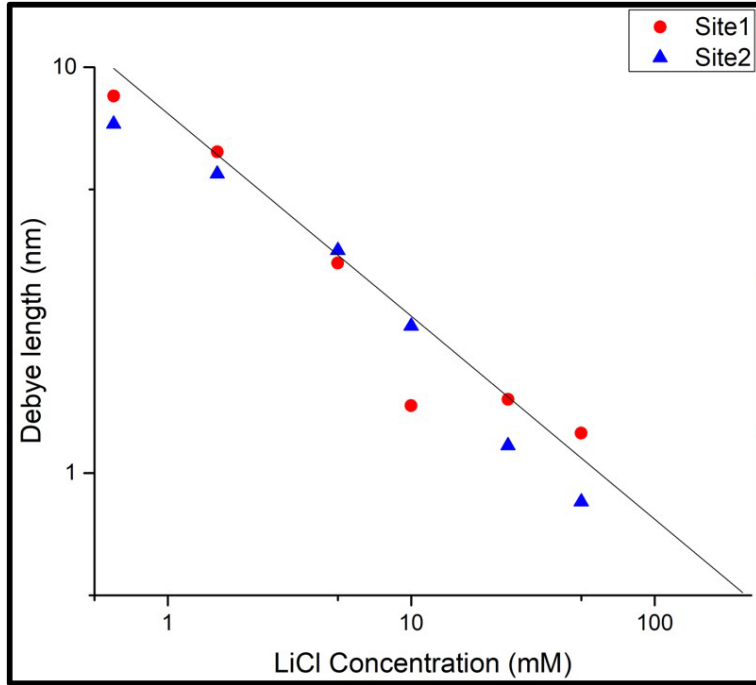


Figure 4.12 A preliminary graph produced to investigate the expected Debye length vs the recorded Debye length at different salt concentrations. The black line indicates the approximated κ , whereas site one and two are two different recording areas on the glass surface.

preliminary data (see fig 4.12). As a result this procedure was used for subsequent experiments. These curves were used for analysis using the following script mechanics.

From these results a selection of the concentrations where an observable Debye length was chosen and processed using all of the techniques outlined in this chapter. This Debye length measurement procedure indicates strongly that our experimental and processing protocol is appropriate. Additionally the influence of contaminants have been reduced to a minimum from said revised protocol.

4.3 Nanowizard

Over the course of the investigation the availability of an alternative AFM became available. When compared to the MFP-1D, the setup is very similar, with one notable exception. This AFM allows for free horizontal control coupled to the AFM head, instead of requiring the operator to disengage each time. Aside from the time saved between changing sites, this allows for techniques such as force mapping to be used (See chapter 2). The setup procedure remained the same as defined before during use with this AFM with any difference being software based, and thus an unnecessary detail for this report.



Figure 4.13 Operation setup for the Nanowizard AFM that was used for force measurements [2].

Fortunately the previously established sample preparation and cleaning procedure were adapted with little difficulty with the experimental throughput considerably increased. The tip speed was set to the previously defined speed, 1 $\mu\text{m}/\text{s}$ as well as the peak force at 8 nN, unless otherwise stated.

4.3.1 Analysis differences for JPK NanoWizard

The output from the Nanowizard was exported from the proprietary JPK file format and refitted to work with the script described above. While the differences in output structure is dramatic, this was handled by a short refactoring script to translate the data into a usable format. The only differences of note between the two is that the JPK format has less significant figures compared to the previous methods.

In the case of force mapping, there are considerably less curves per site. At this point, the previously established curves produced by the MFP-1D for each concentration were used for comparison. Each of the curves is then processed by the script, with a note taken of its x,y μm offset. Afterwards the averaged contact force (for approach) or adhesive force (for retract) is plotted on a heat map. For each heat map a 10×10 grid was processed, with at minimum 3 curves per site taken, with a 1 μm distance between each site. It should be noted that the software processes an entire grid first, which is to say each site is repeated after all sites of the current grid are done.

Chapter 5

Approach force curves

Further to the previous work done in liquid AFM operation, further force curves were taken with a silica-tipped cantilever interacting with a borosilica surface (petri-dish) in a controlled liquid. For each of the curves a controlled concentration of LiCl was added to a 50:50 mix of deionised water and glycerol. Initially the curves were too noisy and unrefined to be taken directly from the machine, thus a script was written and refined over the months from the previous report. For each curve a minimum of 100 curves were binned and averaged into a master curve, with any anomalous lone curves removed. These curves were then analyzed through a python script that corrects the resultant curves from the machine by leveling the noise floor across all curves (*Fig.1*) and defining the contact area linearly (*Fig.2*).

While the initial curves taken on the machine were too noisy, further repeats and refinements to the procedure eventually resulted in 14 averaged curves taken; 7 concentrations with 2 different contact areas taken. Finally these curves were then further tested primarily by analyzing the derivative of the curve and the calculated Debye length taken from the exponent of the curve. Additional further diagnostic curves were produced and checked by eye for every single curve taken into the average, resulting in well over several thousand total curves processed and checked (Fig.3).

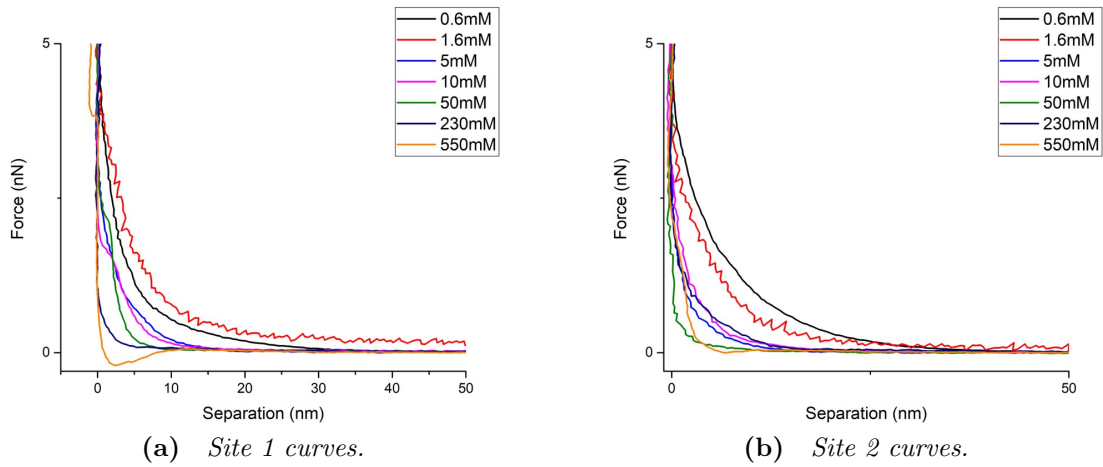


Figure 5.1 The resultant averaged force curves for each of the concentrations. (a) showing the curves taken for the initial contact site and (b) showing the curves taken for the second contact site.

Finally the repulsive force was derived from the curves (the repulsive force applied on the cantilever at contact between the tip and the surface) (Fig.4). This was done by tuning the fitting parameters of the curves, then analysing the resultant curves over and over until an optimal was found. The contact area parameter were then altered over +/-10nm of the visually derived optimal to calculate the range. If a better fit was found, the optimal was recentered, additionally the range was reduced in the case of a clearly incorrect fit.

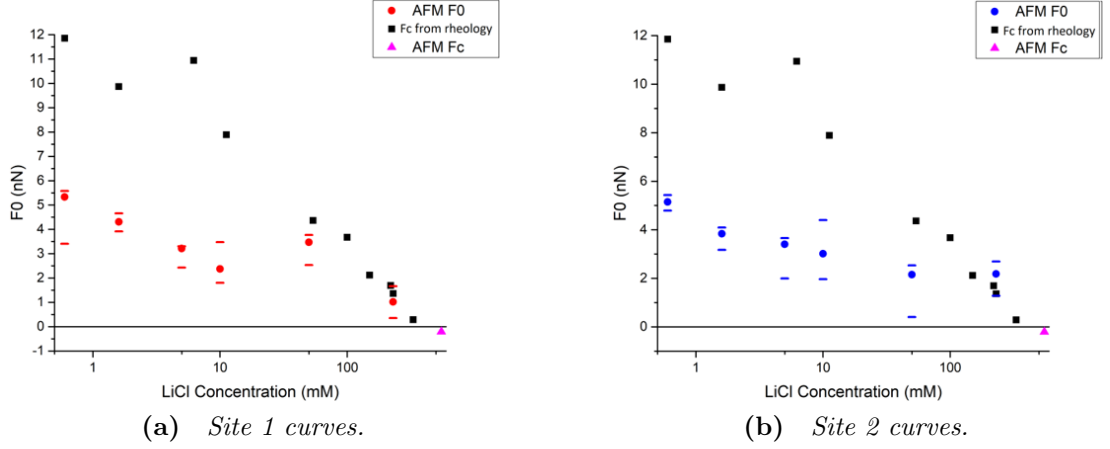


Figure 5.2 The resultant calculated repulsive force between the surface and the tip. The AFM data is compared against data taken from rheology. In the case of 550mM the repulsive forces transition to attractive, corresponding to the onset stress transitioning into yield stress (as seen from rheological data). F_0 is taken from when the curve is within the onset of the contact region, F_c is taken from when the curve bends towards the surface, at the onset of contact (observable in Fig.3. (a) and (b) are site 1 and 2 respectively[33].

Analysis of Silica-silica retract curves

Further analysis is currently being performed on the retract curves utilizing an adapted version of the approach script. This is done in a similar method to the previous, with parameters refined by eye, then the range tested by adding or subtracting 10nm to the contact fitting region. The literature surrounding silica-silica force curves taken in salt usually omit the retract curves, while only a few mention them [4].

[33].

5.1 Introduction

5.1.1 0.6mM

5.1.2 1.6mM

5.1.3 5mM

5.1.4 10mM

5.1.5 25mM

5.1.6 50mM

5.1.7 230mM

5.1.8 550mM

5.2 Effects of hydrodynamics

5.3 Dwell time effects

5.4 pH effects

5.5 Force mapping

Chapter 6

Retract force curves

6.1 Introduction

6.1.1 0.6mM

6.1.2 1.6mM

6.1.3 5mM

6.1.4 10mM

6.1.5 25mM

6.1.6 50mM

6.1.7 230mM

6.1.8 550mM

6.2 Effects of hydrodynamics

6.3 Dwell time effects

6.4 pH effects

6.5 Force mapping

Chapter 7

Force event analysis and conclusions

Chapter 8

Bacterial colloids AFM

8.1 Introduction

In addition to this in liquid force curves were produced from probing bacteria. The possibility of force mapping a bacterial surface was investigated, but ultimately ruled impossible on the current machine. However efforts have been made to procure access to a more suitable AFM (See section 2.1).

8.1.1 AFM tip treatment

Successful adaption and development of the glass treatment to AFM tips was performed. In particular a tip was treated with DCDMS surface coating. This tip was planned to be used with force mapping to investigate the presence of adhesive patches theorized by the group [41] and other literature [35].

8.1.2 Attaching bacteria to a cantilever

8.2 Bacterial force curves

Chapter 9

Conclusion

Bibliography

- [1] Abramovitch, D. Y., S. B. Andersson, L. Y. Pao, and G. Schitter. “A Tutorial on the Mechanisms, Dynamics, and Control of Atomic Force Microscopes.” In *2007 American Control Conference*. 2007, 3488–3502.
- [2] AG, J. I. “NanoWizard NanoOptics AFM - JPK BioAFM: Bruker.”, . <https://jpk.com/products/atomic-force-microscopy/nanowizard-nanooptics>. [Online; accessed 04.05.20].
- [3] Bowen, W., N. Hilal, R. W. Lovitt, and C. J. Wright. “An atomic force microscopy study of the adhesion of a silica sphere to a silica surfaceeffects of surface cleaning.” *Colloids and Surfaces A: Physicochemical and Engineering Aspects* 157, 1: (1999) 117 – 125. <http://www.sciencedirect.com/science/article/pii/S092777579900045X>.
- [4] ———. “An atomic force microscopy study of the adhesion of a silica sphere to a silica surfaceeffects of surface cleaning.” *Colloids and Surfaces A: Physicochemical and Engineering Aspects* 157, 1: (1999) 117 – 125. <http://www.sciencedirect.com/science/article/pii/S092777579900045X>.
- [5] Braga Pier Carlo, R. D. *Atomic Force Microscopy*. Humana press, 2004, 1 edition.
- [6] Butt H-J, J. M. “Calculation of thermal noise in atomic force microscopy.” *Nanotechnology* 6: (1995) 1–7.
- [7] Cannara, R. J., M. Eglin, and R. W. Carpick. “Lateral force calibration in atomic force microscopy: A new lateral force calibration method and general guidelines for optimization.” *Review of Scientific Instruments* 77, 5: (2006) 053,701. <https://doi.org/10.1063/1.2198768>.
- [8] Croft, W. J. *Under the Microscope: A Brief History of Microscopy*, volume 5. World Scientific Publishing, 2006.
- [9] Dabros, T., and T. G. M. van de Ven. “A direct method for studying particle deposition onto solid surfaces.” *Colloid and Polymer Science* 261, 8: (1983) 694–707. <https://doi.org/10.1007/BF01415042>.

- [10] Derjaguin, B., and L. Landau. “Theory of the stability of strongly charged lyophobic sols and of the adhesion of strongly charged particles in solutions of electrolytes.” *Progress in Surface Science* 43, 1: (1993) 30 – 59. <http://www.sciencedirect.com/science/article/pii/007968169390013L>.
- [11] ———. “Theory of the stability of strongly charged lyophobic sols and of the adhesion of strongly charged particles in solutions of electrolytes.” *Progress in Surface Science* 43, 1: (1993) 30 – 59. <http://www.sciencedirect.com/science/article/pii/007968169390013L>.
- [12] Eisenschitz, F., R. London. “ber das Verhltnis der van der Waalsschen Krfte zu den homopolaren Bindungskrften.” *Zeitschrift fr Physik* 60.
- [13] Elbourne, A., K. Voitchovsky, G. G. Warr, and R. Atkin. “Ion structure controls ionic liquid near-surface and interfacial nanostructure.” *Chem. Sci.* 6: (2015) 527–536. <http://dx.doi.org/10.1039/C4SC02727B>.
- [14] van Engers, C. D. *The graphene surface force balance*. Ph.D. thesis, University of Oxford, 2018.
- [15] Eom, N. *Surface Force Measurement between Atomic Layer Deposition Prepared Hafnia Surfaces*. Ph.D. thesis, Department of Applied Mathematics, Research School of Physics and Engineering, The Australian National University, 2017.
- [16] Frasch, H., and H. Menke. “V34: Atomic Force Microscopy.”, 2013. <https://www.henrimenke.com/PPII/V34.pdf>.
- [17] Graham, T. “X. Liquid diffusion applied to analysis.” *Philosophical Transactions of the Royal Society of London* 151: (1861) 183–224. <https://royalsocietypublishing.org/doi/abs/10.1098/rstl.1861.0011>.
- [18] H., E. D. *Basic Principles of Colloid science*. London: Royal Society of Chemistry, 1988, 1st ed. edition.
- [19] Hadjittofis, E., S. Das, G. Zhang, and J. Heng. “Chapter 8 - Interfacial Phenomena.” In *Developing Solid Oral Dosage Forms (Second Edition)*, edited by Yihong Qiu, Yisheng Chen, Geoff G.Z. Zhang, Lawrence Yu, and Rao V. Mantri, Boston: Academic Press, 2017, 225 – 252. Second edition edition. <http://www.sciencedirect.com/science/article/pii/B978012802447800008X>.
- [20] Hansma, P. K., J. P. Cleveland, M. Radmacher, D. A. Walters, P. E. Hillner, M. Bezanilla, M. Fritz, D. Vie, H. G. Hansma, C. B. Prater, J. Massie, L. Fukunaga, J. Gurley, and V. Elings. “Tapping mode atomic force microscopy in liquids.” *Applied Physics Letters* 64, 13: (1994) 1738–1740. <http://dx.doi.org/10.1063/1.111795>.
- [21] J, H. R. *Foundations of colloid science : 2nd ed.* New York: Oxford Uni. Press, 2001, 2nd ed. edition.

- [22] Leite, F. L., C. C. Bueno, A. L. Da Róz, E. C. Ziemath, and O. N. Oliveira. “Theoretical models for surface forces and adhesion and their measurement using atomic force microscopy.” *International journal of molecular sciences* 13, 10: (2012) 12,773–12,856. <https://www.ncbi.nlm.nih.gov/pubmed/23202925>. 23202925[pmid].
- [23] Litton, G. M., and T. M. Olson. “Colloid Deposition Kinetics with Surface-Active Agents: Evidence for Discrete Surface Charge Effects.” *Journal of Colloid and Interface Science* 165, 2: (1994) 522 – 525. <http://www.sciencedirect.com/science/article/pii/S0021979784712586>.
- [24] Lpez-Esparza, R., M. A. Balderas Altamirano, E. Prez, and A. Gama Goic-ochea. “Importance of Molecular Interactions in Colloidal Dispersions.” *Advances in Condensed Matter Physics* 2015: (2015) 8. 10.1155/2015/683716.
- [25] Lderitz, L. A. C. *An AFM study of the interactions between colloidal particles*. Ph.D. thesis, von der Fakultt II - Technischen Universitt Berlin, 2012.
- [26] Moshar, A. “Force Measurements in AFM.”, 2011. https://nanohub.org/resources/11221/download/2011.02.17-AFM_Workshop-L03-Moshar.pdf.
- [27] N, I. J. *Intermolecular and surface forces*. London: Academic Press Limited, 1987, 2nd ed. edition.
- [28] Neas, D., and P. Klapetek. “Gwyddion: an open-source software for SPM data analysis.” *Central European Journal of Physics* 10: (2012) 181–188.
- [29] Ninham, B. “On progress in forces since the DLVO theory.” *Advances in Colloid and Interface Science* 83, 1: (1999) 1 – 17. <http://www.sciencedirect.com/science/article/pii/S0001868699000081>.
- [30] Oliphant, T. “NumPy: A guide to NumPy.” USA: Trelgol Publishing, 2006–. <http://www.numpy.org/>. [Online; accessed 06.05.20].
- [31] plasma, H. “Plasma Cleaning : Henniker Plasma Treatment.”, . <https://plasmatreatment.co.uk/henniker-plasma-technology/plasma-surface-technology/plasma-technology-what-is-plasma-treatment/plasma-cleaning/>. [Online; accessed 084.05.20].
- [32] Richmond, P. “Electrical forces between particles with discrete periodic surface charge distributions in ionic solution.” *J. Chem. Soc., Faraday Trans. 2* 71: (1975) 1154–1163. <http://dx.doi.org/10.1039/F29757101154>.
- [33] Royer, J. R., J. French, J. Sindt, J. Sun, V. Koutsos, and W. C. K. Poon. “Surface forces and particle interactions in shear thickening suspensions.” *In the process of publishing* .

- [34] Savitzky, A., and M. J. E. Golay. “Smoothing and differentiation of data by simplified least squares procedures.” *Analytical Chemistry* 36: (1964) 1627–1639.
- [35] Spengler, C., N. Thewes, P. Jung, M. Bischoff, and K. Jacobs. “Determination of the nano-scaled contact area of staphylococcal cells.” *Nanoscale* 9: (2017) 10,084–10,093. <http://dx.doi.org/10.1039/C7NR02297B>.
- [36] Tabor, D. “Surface forces and surface interactions.” *Journal of Colloid and Interface Science* 58, 1: (1977) 2 – 13. <http://www.sciencedirect.com/science/article/pii/0021979777903666>. International Conference on Colloids and Surfaces.
- [37] Van Rossum, G., and F. L. Drake. *Python 3 Reference Manual*. Scotts Valley, CA: CreateSpace, 2009.
- [38] Verwey, E. J. W. “Theory of the Stability of Lyophobic Colloids.” *The Journal of Physical and Colloid Chemistry* 51, 3: (1947) 631–636. <https://doi.org/10.1021/j150453a001>.
- [39] ———. “Theory of the Stability of Lyophobic Colloids.” *The Journal of Physical and Colloid Chemistry* 51, 3: (1947) 631–636. <https://doi.org/10.1021/j150453a001>.
- [40] Victor J Morris, A. P. G., Andrew R Kirby. *Atomic Force Microscopy for Biologists*. Imperial College Press, 2009, 2 edition.
- [41] Vissers, T., A. T. Brown, N. Koumakis, A. Dawson, M. Hermes, J. Schwarze-Linek, A. B. Schofield, J. M. French, V. Koutsos, J. Arlt, V. A. Martinez, and W. C. K. Poon. “Bacteria as living patchy colloids: Phenotypic heterogeneity in surface adhesion.” *Science Advances* 4, 4. <http://advances.sciencemag.org/content/4/4/eaao1170>.
- [42] van der Waals, J. D. *Over de Continuiteit van den Gas- en. Vloeistofstoestand*. Ph.D. thesis, Univ. Leiden, 1873.
- [43] Wagner, R., A. Raman, and R. Moon. “Transverse Elasticity of Cellulose Nanocrystals Via atomic Force microscopy.” 2010.
- [44] Walz, J. Y. “The effect of surface heterogeneities on colloidal forces.” *Advances in Colloid and Interface Science* 74, 1: (1998) 119 – 168. <http://www.sciencedirect.com/science/article/pii/S0001868697000420>.
- [45] Yoo, S., C.-H. Ji, J.-Y. Jin, and Y.-K. Kim. “Suppression of surface crystallization on borosilicate glass using RF plasma treatment.” *Applied Surface Science* 316: (2014) 484 – 490. <http://www.sciencedirect.com/science/article/pii/S0169433214016110>.

